

Article

Perovskite Type B-CaTiO₃ Coupled with Graphene Oxide as Efficient Bifunctional Composites for Environmental Remediation

Ilknur Altin 

Department of Chemistry, Karadeniz Technical University, 61080 Trabzon, Turkey; ilknurtatlidil@ktu.edu.tr

Abstract: To prepare boron doped perovskite CaTiO₃ nanocubes coupled with graphene oxide (B-CaTiO₃/GO), B-CaTiO₃ photocatalyst was initially synthesized by the solvothermal method and subsequently attached on GO by a simple hydrothermal process. The phase structure and optical features of the prepared materials were efficiently characterized by several techniques. The XRD patterns indicated that boron doping could not give rise to lattice disruption of CaTiO₃. The results of XPS, HRTEM and Raman measurements revealed that the presence of B-CaTiO₃ is anchored on the surface of GO effectively. The morphology of the B-CaTiO₃/5GO was nanocube particles. The photocatalytic capacity of B-CaTiO₃/GO nanocomposites was determined by investigating the degradation of a model dye, methylene blue (MB). Their degradation performance could be enhanced by altering the ratio between B-CaTiO₃ and GO. The most effective GO incorporation is 5 wt%, and at this loading percentage, B-CaTiO₃/GO nanocomposite showed improved photocatalytic activity compared with CaTiO₃ and B-CaTiO₃ photocatalyst, which could be attributed to the synergistic efficacy of the adsorbed MB molecule on the GO followed by their degradation after 180 min of visible light. Additionally, the active species trapping tests confirm the dominant role performed by ·OH and O₂·⁻ during the degradation of MB. The presence of HCO₃⁻ and Cl⁻ indicated moderate prohibitive effect on the degradation of MB, while NO₃⁻ and SO₄²⁻ negatively affected the catalytic activity in a non-significant way. In brief, the results of this study show that boron doped perovskite-type semiconductor catalysts by combining with graphene has significant efficiency in the removal of MB from aqueous solution, which can be employed as effective photocatalyst materials for the treatment of other organic pollutants.

Keywords: perovskite; boron doped CaTiO₃; visible light induced photocatalysis; methylene blue



Citation: Altin, I. Perovskite Type B-CaTiO₃ Coupled with Graphene Oxide as Efficient Bifunctional Composites for Environmental Remediation. *Processes* **2023**, *11*, 3191. <https://doi.org/10.3390/pr11113191>

Academic Editors: Mohammad Boshir Ahmed, Md Ashraf Hossain, Mohammad Shamsuddin Ahmed, Jivan Thakare and Mostafa Y. Nassar

Received: 19 September 2023

Revised: 18 October 2023

Accepted: 6 November 2023

Published: 8 November 2023



Copyright: © 2023 by the author. Licensee MDPI, Basel, Switzerland. This article is an open access article distributed under the terms and conditions of the Creative Commons Attribution (CC BY) license (<https://creativecommons.org/licenses/by/4.0/>).

1. Introduction

Water pollution is a significant concern that arises from the contamination of water bodies with harmful substances. Dye pollution from textile dyes represents the main source of water pollution from colored compounds. The contamination of wastewater with these dyes uses up dissolved oxygen, affecting aquatic life, and causes environmental problems [1,2]. Methylene blue (MB) is a synthetic dye commonly used as a colorant in paints and other applications, and its release into water bodies can have detrimental effects on the environment and human health [3].

Solar light driven photocatalysis is one of the encouraging methods for environmental remediation in a more environmentally friendly approach [4–6]. Semiconductor-based photocatalysis has been widely studied and applied in various environmental applications, particularly in the field of environmental pollution remediation [7,8]. The basic principle of semiconductor photocatalysis involves the absorption of photons with energy equal to or greater than the band gap of the semiconductor. This results in the formation of e⁻/h⁺ pairs which then react with the oxygen and hydroxyl ions to produce radical species that can decompose the water pollutants on the surface of catalyst particles easily and rapidly [9,10].

In this context, several semiconductor-based processes and their composites have been widely studied and applied in various environmental applications [11–13]. Among the wide range of photocatalytic samples synthesized to date, perovskite-based semiconductors of the form ABO_3 have recently taken widespread attention because of their great properties such as electron mobility, stable photo-electrochemistry properties, band gap tunability, and high thermal and photocorrosion stability [14–18]. Generally, in this crystal structure, the A cation typically has a larger size, and the B cation has a smaller size, relative to the oxygen ions. The size difference gives rise to the aforementioned properties of perovskite oxides [19–21]. Thus, this n-type semiconductor can be a good substitute for industrial catalyst TiO_2 , as it has a more negative conduction band potential than the TiO_2 , which is widely and effectively used. Particularly, calcium titanate ($CaTiO_3$) with a perovskite crystal form has been used in several areas containing environmental remediation, energy conversion, biomedical application, and industrial processes [22–25]. Although $CaTiO_3$ is an effective perovskite material used in a wide range of fields, due to its large band gap (~3.5 eV) and low quantum efficiency, its catalytic performance is restricted to UV irradiation only [26,27]. Also, photo-formed electron-hole pairs can recombine quickly, which is another concern that adversely affects photocatalytic performance [28,29]. Generally, the most important points for achieving the high photocatalytic performance of $CaTiO_3$ are the efficient separation of photoinduced charge carriers and the need to expand the absorption into the visible range. In this regard, several attempts have been made in which graphene-based supporting materials are utilized to overcome these issues in recent years [30–32]. The synergistic mutual effect of graphene-coupled composite and semiconductor can improve different stages of photocatalysis: (i) the light absorption range can shift to the red region to make better use of sunlight; (ii) the induced electrons can be effectively moved to sp^2 -hybridized carbon structure, so quenching e^-/h^+ recombination; (iii) it can increase the adsorption of pollutants with the large specific surface area since the adsorption of pollutants on the $CaTiO_3$ surface is a key point in the aqueous phase [33–35]. So, graphene-semiconductor nanostructured materials are of great interest and have maintained to be studied recently to improve catalytic activity. Kumar et al. prepared nitrogen doped $CaTiO_3$ (NCT)-reduced graphene oxide (RGO) catalyst with very effective visible light induced catalytic performance for the removal of methylene blue and assigned this to the efficient interaction of the adsorption of MB on the graphene and the subsequent decomposition [35]. Xian et al. prepared $CaTiO_3$ -graphene nanocomposites by stirring $CaTiO_3$ particles and graphene into ethanol, followed by drying with improved UV-light-driven photocatalytic degradation for methyl orange (MO) [36]. Chen et al. reported magnetically recoverable $CaTiO_3$ /RGO/ $NiFe_2O_4$ ternary material with increased degradation for methylene blue and rhodamine B contaminants under the sunlight irradiation [37]. Lalan et al. synthesized Ag- $CaTiO_3$ @rGO nanocomposite with enhanced photocatalytic degradation for the sulforhodamine B under natural sunlight and attributed this to the synergistic effect of plasmon-driven visible light because of Ag and increased adsorption and electron-transport features due to rGO [38]. Luo et al. reported $CaTiO_3$ integrated with rGO composites with increased photocatalytic capacity towards the removal of MO [39]. Also, by doping with foreign atoms with $CaTiO_3$, studies have reported visible light activity for degradation of pollutants. Boron doping is an alternative way, which is documented in the literature to obtain photocatalysis under visible irradiation [40,41]. Recently, in a study reported by Wu et al., it was stated that compared to other dopants, boron can be immobilized much more easily into the graphene structure by substituting the carbon atom owing to its theoretical size compatibility. Due to the electron-deficient nature of boron, this doping can improve its p-type conductivity properties, allowing its application in photocatalysis. Therefore, the active sites of boron can become electron acceptors. Unlike the n-type transfer property, the boron atom, which acts as a strong charge acceptance center, ensures the p-orbital and supports charge transfer, which is useful for the photocatalysis procedure [42]. However, there are no such studies in the case of $CaTiO_3$ perovskite catalyst according to the literature review so far.

With this perspective, this study reports the preparation, characterization, and comparative study of the photocatalytic activity of series of B-CaTiO₃/GO nanocomposites (with 1 to 15 wt% of GO). The solvothermal method was performed to synthesize B-CaTiO₃ photocatalyst and then the prepared GO were decorated on it using the hydrothermal process. Due to its easy accessibility, and cost-effective and versatile application in industry, the boron element was selected for this study. The photocatalytic performances of the B-CaTiO₃/GO nanocomposites were investigated for the removal of MB under the irradiation of visible light. The effect of loading quantity of GO on the light absorbency and photocatalytic activity was studied. The physical features of the most efficient nanocomposite (namely B-CaTiO₃/5GO) were deeply characterized. For the same photocatalyst, the effect of different experimental conditions such as pH, initial MB concentration, catalyst mass, humic acid (natural organic substance (NOM)), and inorganic ions has been assessed as much as its stability and reusability. Additionally, a possible photocatalysis mechanism has been proposed by trapping tests. The notable catalysis results and recyclability of the B-CaTiO₃/5GO composite material can be a sign of a potential effective material in the photocatalysis system for environmental remediation. Therefore, the results of this study may be helpful for the plan of visible/solar irradiation induced photocatalyst and reusable perovskite-based catalysts for many industrial applications.

2. Materials and Methods

2.1. Materials

Titanium (IV) butoxide (Ti(OC₄H₉)₄), Ca(NO₃)₂·4H₂O, H₃BO₃, PEG4000, NaOH, HCl, H₂SO₄, NaNO₃, KMnO₄, H₂O₂ (35% in water), NaHCO₃, Na₂SO₄, KCl, humic acid sodium salt, isopropyl alcohol, benzoquinone, and ethylenediaminetetraacetic acid disodium salt dehydrate were used from Sigma-Aldrich company (Bengaluru, India). Deionized water utilized during the whole study was obtained by an ultra-filtration system (1.47 μs/cm at 25 °C).

2.2. Synthesis and Characterization

2.2.1. Synthesis of CaTiO₃ and B-CaTiO₃

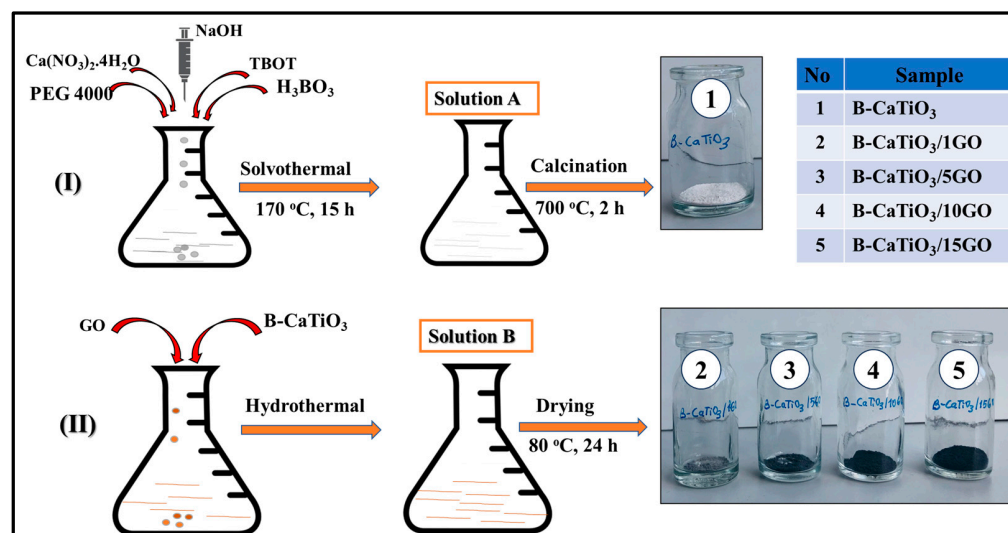
The samples were synthesized using NaOH as a mineralization reagent through the solvothermal method [43]. In a typical procedure, 2.5 mL Ca(NO₃)₂·4H₂O (4 M) and 2.5 mL H₃BO₃ (2 M) were dissolved in 172 mL of PEG 4000 solvent with constant stirring. Then, 3.3 mL of Ti(OC₄H₉)₄ was added dropwise to the above solution under constant stirring. To this suspension, 22 mL of NaOH solution (10 M) was added dropwise and stirred for a further 2 h. Subsequently, the milky white suspension was solvothermally treated at 180 °C for 15 h. The resulting product was then washed with ethanol and DI water, centrifuged, and dried at 80 °C. After drying, the resultant material was further sintered at 700 °C for 2 h. The synthesis of CaTiO₃ catalyst was similar to the above procedure without adding H₃BO₃.

2.2.2. Synthesis of Graphene Oxide

Graphene oxide (GO) was synthesized by graphite through the Hummers method [44]. Briefly, 2 g of graphite flakes (from Kropfmuhl GmbH, Hauzenberg, Germany) were dissolved with 92 mL of H₂SO₄ (conc.) and then of 2 g of NaNO₃ was put in it under stirring in ice bath for 30 min until it to about 0 °C. Moreover, 12 g of KMnO₄ was added very slowly to the above solution and maintained at 35 °C and stirred for 2 h. Then, 140 mL of DI water was slowly added to this mixture and the final suspension was left mixing at 95 °C for a further 1 h in the silicon oil bath. This mixture was then cooled to room temperature and then 400 mL of DI water was added and 14 mL H₂O₂ was then added slowly to get the yellow color of the mixture. Then, the resulting yield was washed with DI water and centrifuged at 10,000 rpm for 10 min. Eventually, GO powder could be prepared by drying at room temperature.

2.2.3. Synthesis of B-CaTiO₃/GO Composites

The B-CaTiO₃/GO composites were prepared in an easy hydrothermal way. In a typical procedure, a certain amount of GO (which is equal to 1, 5, 10, and 15% of B-CaTiO₃ mass, respectively) was ultrasonicated in 10 mL of DI water. Then, 250 mg of B-CaTiO₃ was also dispersed in 10 mL of DI water. Then, both suspensions were mixed, ultrasonically dispersed for 30 min, and stirred for 24 h to get B-CaTiO₃/GO photocatalysts. Finally, the resulting suspension was dried overnight at 70 °C (Scheme 1).



Scheme 1. The preparation processes of B-CaTiO₃ nanopowder (I) and B-CaTiO₃/GO nanocomposites (II).

2.2.4. Material Characterization

The crystallographic studies of the prepared materials were performed in the 2θ range from 10–90° by using a PANanalytical Empyrean diffractometer with a CuKα radiation (λ = 0.1542 nm). Raman spectroscopic analyses were carried out with a WITech alpha 300R using a 532 nm laser for excitation. Surface morphology was assessed by field emission scanning electron microscopy (FESEM-EDS, Zeiss Sigma 300, St. Louis, MO, USA) and high-resolution transmission electron microscopy (HR-TEM FEI TALOS F200S at 200 kV). X-ray photoelectron spectroscopic (XPS) analysis was carried out on a Thermo Scientific (Waltham, MA, USA) K-Alpha having an Al-Kα radiation micro-focused monochromator with variable spot size (30–400 μm in 5 μm steps) to detect the elemental composition of the material. The ultraviolet-visible (UV-vis) diffuse reflectance spectra (DRS) were measured using a UV-VIS-NIR spectrophotometer (Shimadzu UV-3600 Plus, Kyoto, Japan). The photoluminescence (PL) spectra were measured with Edinburgh Instruments FLSP920 fluorescence spectrometer. The Brunauer–Emmett–Teller (BET) specific surface area (S_{BET}) and nitrogen adsorption–desorption isotherms were measured at 77 K on a Micromeritics 3Flex Version 4.02. The isoelectric point, pH_{pzc}, was determined using Zeta-sizer equipment (Malvern Zetasizer Nano ZSP, Malvern, UK). The total organic compound (TOC) analysis was carried out by Shimadzu TOC-L.

2.3. Photocatalytic Activity Study

The photocatalytic performance of the prepared materials was investigated through MB dye removal under visible irradiation (450 nm, the light source was fabricated with 5 Philips Mercury (Hg) lamps-TL-K 40W/10R ACTINIC BL REFLECTOR, 2.3 mW/cm²). In a typical reaction, 50 mg of each catalyst was put in 50 mL of 10 mg L⁻¹ aqueous solution of MB and stirred for 30 min in the absence of light to achieve the adsorption–desorption equilibrium between MB and the catalyst surface. Photodegradation of the pure MB in the absence of the catalyst or dark experiments in the presence of the catalyst was also evaluated under the same experimental conditions as control experiments. After definite

time intervals of 30 min, 4 mL of the suspension taken out from the test quartz tube was centrifuged to remove any residual solid catalyst particles for 5 min at 10,000 rpm. After separation, the supernatant was monitored at $\lambda = 668$ nm using a spectrophotometer and the amount of dye in the supernatant was calculated in relation to the reaction time. The removal percentage (%) of dye was estimated using the formula:

$$\text{Degradation}(\%) = (1 - C_t/C_0) \times 100 \quad (1)$$

Here C_0 is the initial MB concentration, and the MB concentration after sample irradiation is C_t . Separated catalysts were simply washed with DI water and dried at 80 °C, and then kept for reusability experiments. Moreover, effects of some experimental parameters such as pH, pollutant concentration, catalyst mass, and water matrix have been investigated as much as reusability of the best composite B-CaTiO₃/5GO. The effect of anions on photocatalytic activity was studied for the best composite B-CaTiO₃/5GO via the introduction of NaNO₃, NaHCO₃, Na₂SO₄, and KCl, respectively. The effect of the presence of humic acid on the degradation efficiency was also evaluated to simulate water more realistically. In order to further usability of best sample B-CaTiO₃/5GO as a catalyst for water treatment, the dye degradation was studied by performing the decomposition in sea water, tap water, and drinking water-spiked MB. Furthermore, the effect of pH on the photocatalytic activity was evaluated by adjusting the pH of the reaction solution with 0.1 M NaOH or 0.1 M HCl solutions. To determine the generation of different reactive oxygen species (ROS), ethylenediaminetetraacetic acid, benzoquinone, and isopropyl alcohol were evaluated.

3. Results and Discussions

3.1. Structural and Morphological Analysis

The X-ray diffraction (XRD) analysis was carried out on GO, CaTiO₃, B-CaTiO₃, and B-CaTiO₃/GO nanocomposites to predict the crystal structure and phase composition and the XRD patterns are shown in Figure 1.

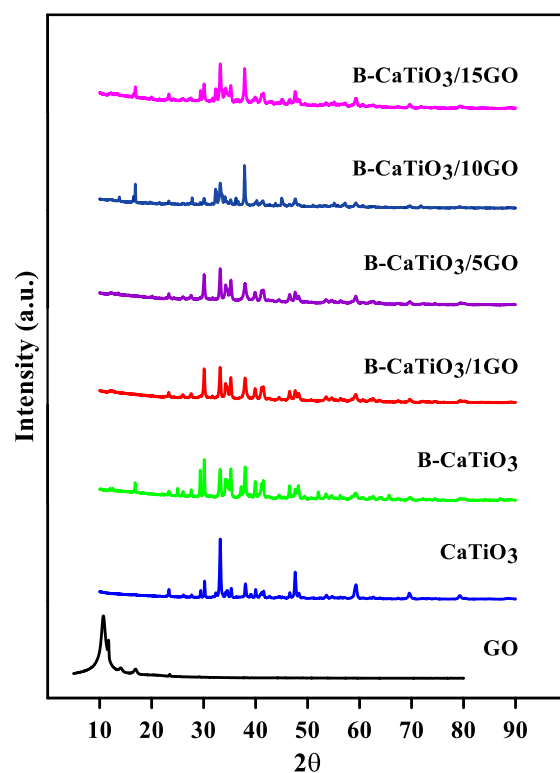


Figure 1. XRD patterns of the prepared photocatalysts.

The major peak of GO appears at $2\theta = 10.8^\circ$ which can be attributed to the oxidation of graphite into GO. The characteristic peak of GO at 10.8° could not be seen in the XRD pattern of the B-CaTiO₃/GO composites. This can be attributed to the fact that a big proportion of GO layers in the nanocomposite are intercalated via B-CaTiO₃ particles, aggregation in an irregular pattern, and a low amount of GO in the composites. Meanwhile, there is no observable peak of boron ion in the XRD, which may be because of the small weight ratio of boron incorporated into the lattice of CaTiO₃. However, more intense peaks were obtained compared to the peaks of CaTiO₃. All possibilities can also lead to relatively weak diffraction intensity of both GO and boron in comparison to the other peaks. All the XRD peaks of nanocubes catalysts can be indexed to the orthorhombic phase (JCPDS card no. 82-0228), indicating the purity and orthorhombic phase of CaTiO₃ [43]. It can be seen in Figure 1 that the intensities of the fundamental phases of CaTiO₃ are not significantly affected and the XRD patterns of modified CaTiO₃ and pure CaTiO₃ are similar. Since the ionic radius of the Ca²⁺ is bigger than the B³⁺ ion (180 pm and 85 pm, respectively), this shows the substitution of Ca²⁺ sites with B³⁺ in the crystalline lattice of CaTiO₃ resulting in some internal strain [45]. Furthermore, the average crystallinity of CaTiO₃, B-CaTiO₃, B-CaTiO₃/1GO, B-CaTiO₃/5GO, B-CaTiO₃/10GO, and B-CaTiO₃/15GO were computed using the Scherrer equation [46] as 28.0, 25.2, 26.9, 27.3, 26.4, and 27.8 nm, respectively. In all situations, a nanometric distribution of B-CaTiO₃ catalyst is seen, and it is estimated that the crystal size decreases as the weight percentage of GO loaded increases, resulting in a good B-CaTiO₃/GO interaction. Also, B-CaTiO₃/GO composites with different mass percentages of GO indicated XRD peaks similar to that of B-CaTiO₃ without affecting the main structure in all catalysts powder. Considering the photocatalytic results, structural and morphological analyses were performed only on the best photocatalyst, namely B-CaTiO₃/5GO. The optical properties of CaTiO₃, B-CaTiO₃, and B-CaTiO₃/5GO were determined by UV-visible DRS in the range of 200–800 nm and their band gap energies can be estimated using the formula:

$$E_g = 1240 / \lambda_g \quad (2)$$

where E_g is optical band gap energy, and λ_g is the absorption of the catalyst [47].

As can be shown in Figure 2, the neat CaTiO₃ has an adsorption edge at 372.3 nm and the band gap energy was calculated to be 3.33 eV and accordingly, there is no absorption in the visible range. Since the incorporation of boron into the structure remarkably has an effect on the electronic structure of CaTiO₃, exhibiting a shift to about 414.4 nm, this ascribes to the band gap of 2.99 eV and an absorption near the visible region is obtained. This reduction in the band gap indicates that additional energy levels excited by B-doping occur above the valence band (VB) of the CaTiO₃ and shift its absorption to the visible region. The red shift observed in the absorption wavelength of B-CaTiO₃ compared to CaTiO₃ also shows the successful doping of B into the lattice structure of CaTiO₃. In addition, the absorption edge of B-CaTiO₃/5GO is observed at 434.4 nm and its calculated band gap energy is 2.85 eV. Hence, the absorption in the visible range is increased for B-CaTiO₃/5GO composite as compared to the pure CaTiO₃ and B-CaTiO₃. This suggests the strong photoactivity of this sample under the visible light. This data is compatible with the incorporation of graphene, which increases the visible region absorption and consequently increases the catalytic capacity [48]. Hereby, the DRS data obviously shows that the synergistic effect of both B and GO loading in CaTiO₃ bricks increases the absorption of the visible range by the catalysts and accordingly the photocatalytic activity was also improved. Attou et al. [49] investigated the band gaps of undoped and B-doped CaTiO₃ semiconductor perovskites with Density Functional Theory (DFT) and Boltzman transport theory (BoltzTraP) using the full potential linearized augmented plane wave (FP-LAPW) method with the GGA-PBE approach. They stated that by incorporating B into CaTiO₃, the band gap efficiently decreased and as a result, the ability to absorb visible light increased. They demonstrated that the conduction band minimum (CBM) for pure CaTiO₃ is the hybridization of Ca 2s, 4p, Ti 3p, 3d, and O 2s, 2p orbitals. In their study, incorporating B into a CaTiO₃ lattice resulted in the hybridization of CBM orbitals with B 2s, 2p, and

accordingly, the energy of the B 2s orbital decreased and the energy band gap decreased. Raman analyses were carried out to confirm the presence of GO and B-doped CaTiO₃. As can be seen in Figure 3, the curve of B-CaTiO₃ exhibits typical peaks at 79.1 cm⁻¹, 137.03 cm⁻¹, and 184.2 cm⁻¹ corresponding to the vibrations of B-CaTiO₃ [50].

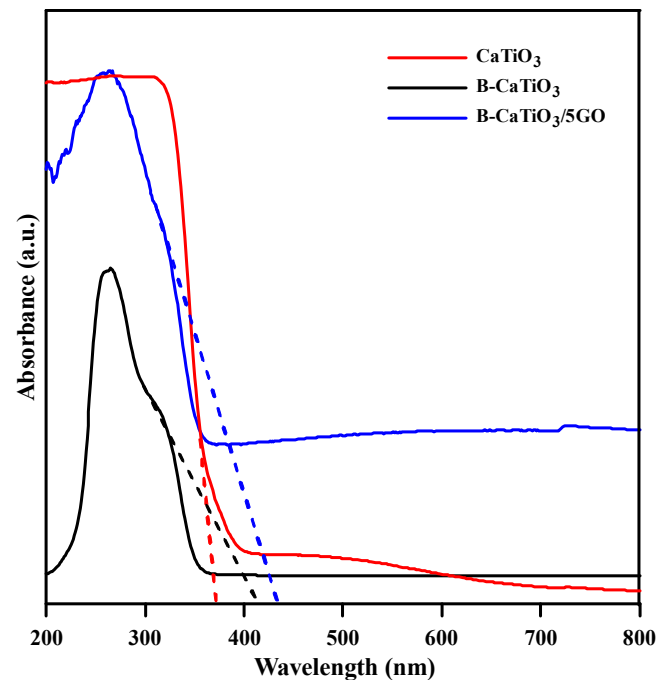


Figure 2. UV-visible diffuse reflectance spectra (DRS) of CaTiO₃, B-CaTiO₃, and B-CaTiO₃/5GO.

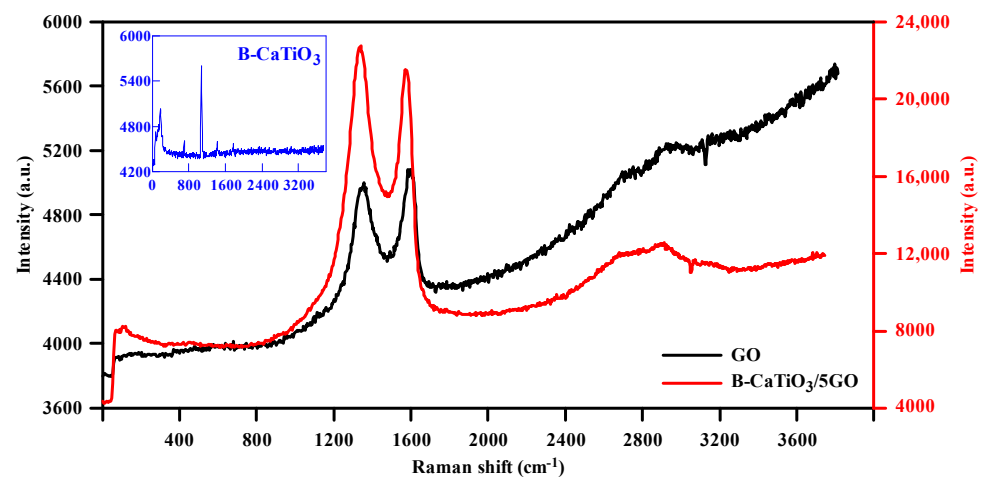


Figure 3. Raman spectra of B-CaTiO₃ (insert), GO (black line), and B-CaTiO₃/5GO (red line).

The Raman band located at 184.2 cm⁻¹ is corresponding to the motion of Ca²⁺ ions [51,52]. Moreover, the bands in GO at 1339.8 cm⁻¹ and 1579.6 cm⁻¹ show the defect-pertaining D and the graphitic G bands. The G band is based on the vibration of sp² carbon atoms in the layer and the D band shows the breaking of sp² hybridized C=C bonds to sp³ hybridized C-C bonds during the oxidation of graphite [53]. Photoluminescence (PL) analysis was performed to examine the effect of GO loading in B-CaTiO₃/5GO composite and the obtained PL spectra of B-CaTiO₃ and B-CaTiO₃/5GO catalysts are shown in Figure 4. Figure 4a–d shows the PL spectra of bare CaTiO₃ (a), B-CaTiO₃ (b), B-CaTiO₃/5GO (c) catalysts, and GO (d) in the wavelength range between 300 and 1000 nm with excitation wavelength of 532 nm. The catalysts samples displayed strong luminescence under UV

excitation. CaTiO_3 exhibits an emission intensity at 652 nm. Simultaneously, local vibrations in the lattice structure and thermal vibrations resulted in luminescence spectra with a broad band [54,55]. The PL intensity of $\text{B-CaTiO}_3/5\text{GO}$ at 652 nm was higher than B-CaTiO_3 and CaTiO_3 under the same measuring conditions. Figure 4d shows the PL spectra of GO. Three emission peaks located at approximately 452, 654, and 687 nm, respectively, are observed in GO. This suggests that the doping of boron and incorporation of GO caused an enhancement of the emission properties [55]. To understand more details of the surface feature of the $\text{B-CaTiO}_3/5\text{GO}$, the XPS analysis is carried out.

The survey spectra of the $\text{B-CaTiO}_3/5\text{GO}$ composite in Figure 5a shows all the elements of Ca, Ti, O, B, and C arriving from the composite sample. The high-resolution Ti 2p is seen in Figure 5b, the peaks located at 460.29 and 465.79 eV for Ti 2p_{3/2} and Ti 2p_{1/2}, respectively, of Ti⁴⁺ of CaTiO_3 [56]. As we see from Figure 5c, the B 1s XPS spectrum has three different peaks at 190.72, 194.04, and 200.43 eV, respectively. The peak at 190.72 eV shows the presence of boron that is probably interstitially waded in the CaTiO_3 with Ti-O-B structure, that at 194.04 eV represents the B-O-B groups, typical of the H_3BO_3 or B_2O_3 phase, that at 200.43 eV could be assigned to the boron doped into TiO_2 by occupying O sites to generate O-Ti-B bond [57,58]. From Figure 5d, the O 1s divides into two peaks of 531.08 eV and 533.46 eV, which can be attributed to the oxygen present in the lattice and surface -OH groups, respectively [59]. The XPS spectrum of Ca²⁺ is given in Figure 5e, two typical peaks at 351.97 eV and 348.82 eV are attributed to Ca 2p_{1/2} and Ca 2p_{3/2}, respectively [56]. Furthermore, as revealed in Figure 5f for C 1s, the binding energies at 291.30 eV and 286.88 eV for the partially oxidized carbonaceous moieties (C-O bonds) and C-C bonds, respectively [60]. To examine the impact of GO nanolayers on the surface area of CaTiO_3 and to explore the impact of GO on improving the photocatalytic capacity of the $\text{B-CaTiO}_3/5\text{GO}$ composite, the BET surface area of B-CaTiO_3 and $\text{B-CaTiO}_3/5\text{GO}$ samples has been investigated. Figure S1 in Supplementary Materials shows the N₂ adsorption–desorption isotherms for B-CaTiO_3 and $\text{B-CaTiO}_3/5\text{GO}$ heterojunction. As given in Table 1, the BET surface area of the B-CaTiO_3 and $\text{B-CaTiO}_3/5\text{GO}$ are 0.0573 m²/g and 3.9303 m²/g, respectively. The total pore volumes of B-CaTiO_3 and $\text{B-CaTiO}_3/5\text{GO}$ materials are 0.0012 cm³/g and 0.0350 cm³/g, respectively. Regarding the pore size, the pore width of $\text{B-CaTiO}_3/5\text{GO}$ (10.53 nm) is smaller than that of B-CaTiO_3 (202.76 nm). After GO loading on B-CaTiO_3 , the BET surface area of the $\text{B-CaTiO}_3/5\text{GO}$ composite was increased to 3.9303 m²/g, which is larger in comparison to that of B-CaTiO_3 . Thus, $\text{B-CaTiO}_3/5\text{GO}$ heterojunction catalyst with the high surface area supplies further reaction area for the adsorption and subsequent degradation of MB dye and therefore results in the improvement of photocatalytic performance.

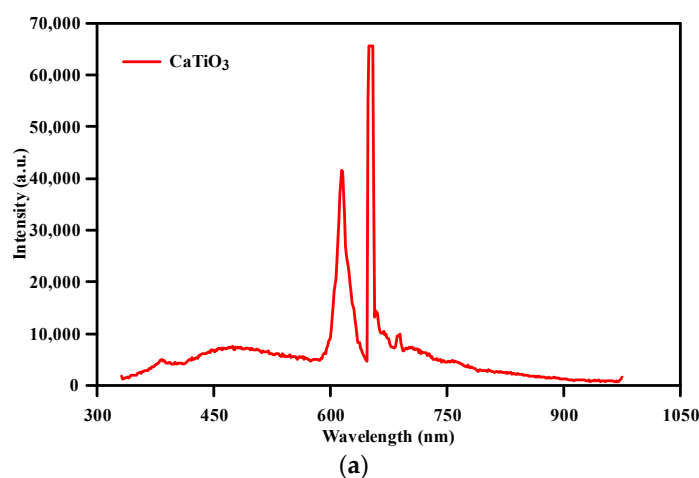


Figure 4. Cont.

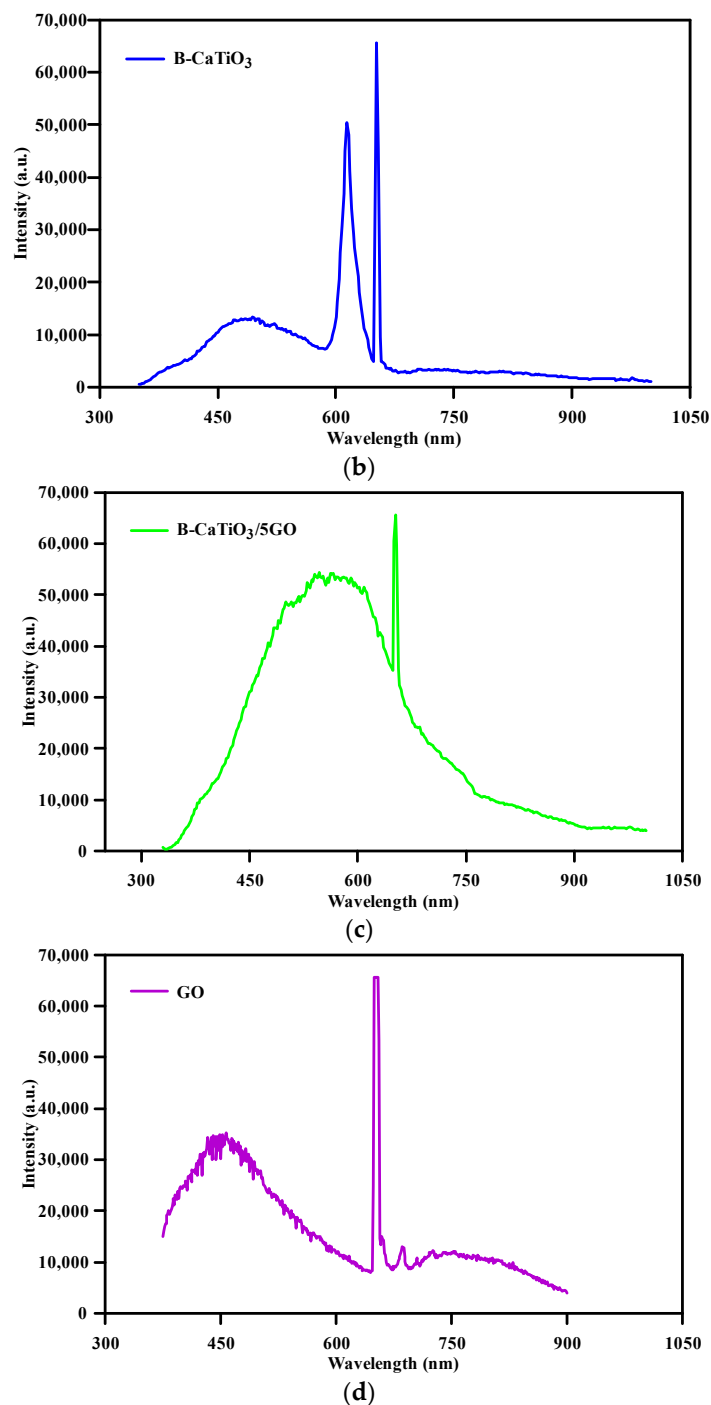


Figure 4. PL spectra for CaTiO_3 (a), B-CaTiO_3 (b), $\text{B-CaTiO}_3/5\text{GO}$ (c), and GO (d).

Table 1. Structural characteristics of B-CaTiO_3 and $\text{B-CaTiO}_3/5\text{GO}$ catalysts.

Catalysts	S_{BET}	^a PS, Pore Size (nm)	^b V_{pore} (cm^3/g)
B-CaTiO_3	0.0573 m^2/g	202.76 nm	0.0012 cm^3/g
$\text{B-CaTiO}_3/5\text{GO}$	3.9303 m^2/g	10.53 nm	0.0350 cm^3/g

^a Average pore diameter calculated from BJH desorption average pore width (4V/A). ^b Single point total pore volume at the relative pressure of ca. 0.966.

The general morphology of B-CaTiO_3 and $\text{B-CaTiO}_3/5\text{GO}$ catalysts was investigated using the FESEM-EDS technique. The FESEM images taken at different magnifications and perspective of B-CaTiO_3 are shown in Figure 6a–c, which shows irregular cube-like

morphology. Also, the FESEM images taken at different magnifications and perspectives of B-CaTiO₃/5GO are shown in Figure 6d–f. As shown in Figure 6d–f, the formation of GO nanolayers in the form of nanobelts can be seen, and the B-CaTiO₃ particles deposited on GO sheets, thus confirming the successful heterojunction formation, which indicates B-CaTiO₃ particles and GO sheets were not isolated from each other. In this manner, this can be advantageous for separation of e⁻/h⁺ pairs, facilitating their transfer and reducing aggregation of nanoparticles. Figure 6g presents EDS spectra of Ca, Ti, O, B, and C element loaded on B-CaTiO₃/5GO composite material confirming the presence of all the constituent elements. Moreover, these results also show that the heterostructure formed by B-CaTiO₃ and GO was formed using the hydrothermal method, which is a simple economical preparation. Further, the HR-TEM images of B-CaTiO₃/5GO with different magnifications are shown in Figure 7a–f. The SAED pattern given in Figure 7g suggests the presence of B-CaTiO₃ crystalline structure [61].

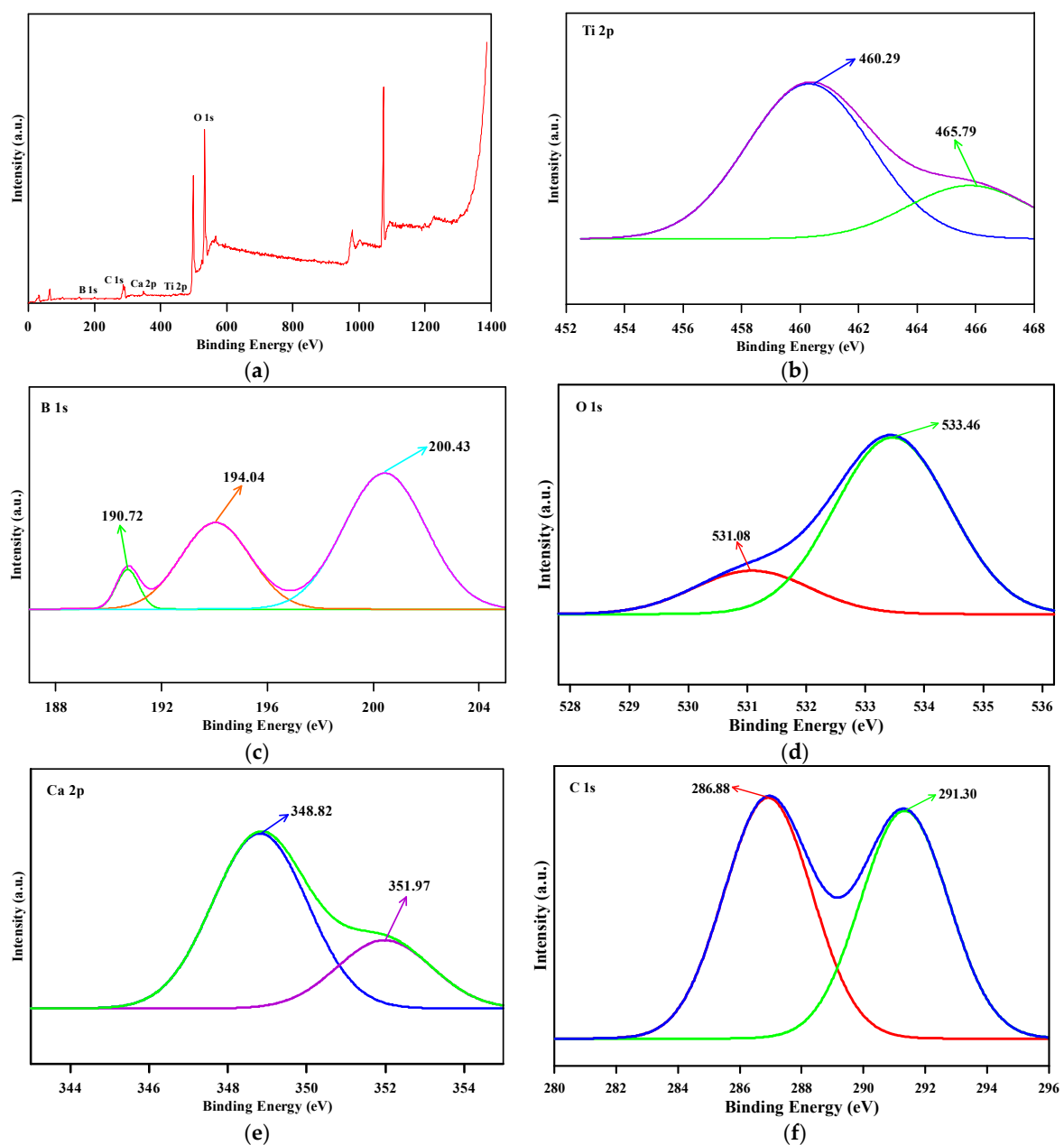


Figure 5. XPS survey spectra of the B-CaTiO₃/5GO (a), XPS spectra for Ti 2p (b), B 1s (c), O 1s (d), Ca 2p (e), and C 1s (f).

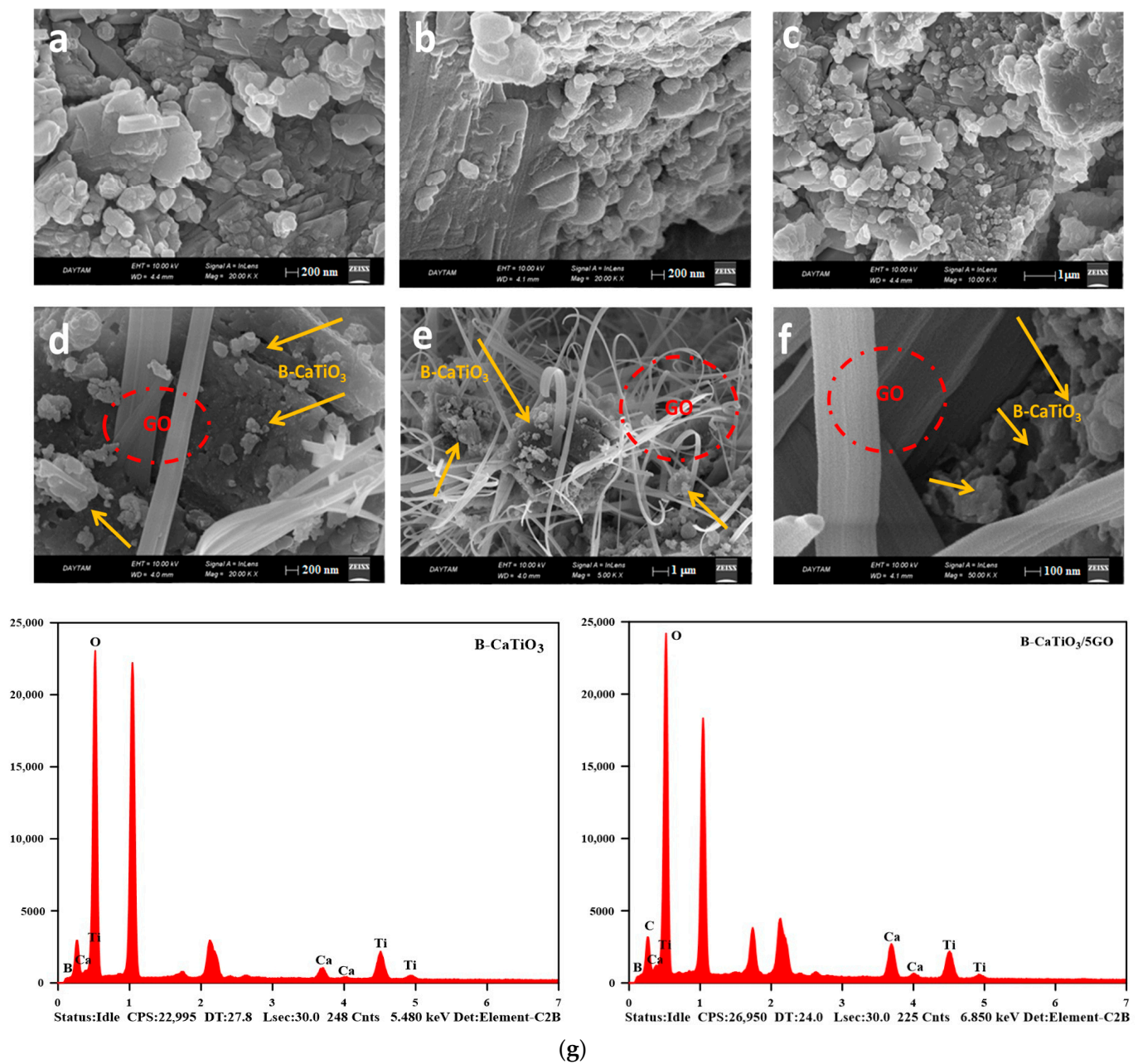


Figure 6. FE-SEM images for B-CaTiO₃ (a–c), B-CaTiO₃/5GO (d–f), and EDS spectra (g).

3.2. Photocatalytic Activity Studies

The photocatalytic performance of the CaTiO₃, B-CaTiO₃, and all B-CaTiO₃/GO nanocomposites was studied by evaluating the removal of methylene blue (MB) dye pollutant under visible irradiation. For comparison purposes, control tests, including dark tests (with catalyst, no light) and light without catalyst, were performed under the same parameters. The impact of GO amounts on the photocatalytic activities of B-CaTiO₃/GO composites was studied. The corresponding results are shown in Figure 8.

As indicated in Figure 8a, the adsorption removal percentages of MB (experiments in the dark) over the CaTiO₃, B-CaTiO₃, B-CaTiO₃/1GO, B-CaTiO₃/5GO, B-CaTiO₃/10GO, and B-CaTiO₃/15GO were 6.8%, 10.8%, 33.9%, 39.6%, 41.8%, and 45.3% respectively. The best adsorption removal efficiency was obtained for B-CaTiO₃/15GO composite (45.3%). It was observed that the adsorption of MB pollutant on the graphene increased as the amount of GO increased. These improved adsorptions of dye molecules can be assigned to the large surface area of GO modified with the perovskite photocatalyst and more dye

molecules are adsorbed on the surface of the B-CaTiO₃/GO composite to overcome the resistance of all mass transfer with the increase in MB concentration. Figure 8b shows the photocatalytic activities of the photocatalysts that are studied using the visible light driven photocatalysis for MB degradation. Initially, it was found that the photodegradation of the pure MB solution in the absence of the photocatalyst is only around 5.4% in a time of 180 min, signifying its high photo-stability. The first reduction in the degradation rate of MB increases with the increase in the GO amount, which could be attributed to the improved adsorption during the adsorption–desorption equilibrium for 30 min to provide adsorption–desorption equilibrium. Also, the decrease in absorption is due to the degradation of MB. After 180 min of visible light, the degradation rates (%) of MB calculated for CaTiO₃, B-CaTiO₃, B-CaTiO₃/1GO, B-CaTiO₃/5GO, B-CaTiO₃/10GO, and B-CaTiO₃/15GO were 10.1%, 31.3%, 75.8%, 87.4%, 82.3%, and 77.6%, respectively. As shown in Figure 8b, pure CaTiO₃ shows relatively low catalytic activity (10.1%) due to its weak visible light utilization and high recombination of e⁻/h⁺ pairs. Furthermore, the degradation of MB of B-CaTiO₃ catalyst is slightly increased to 31.3%. Notably, the degradation rate of MB with B-CaTiO₃/5GO is significantly enhanced to 87.4%, which is around 8.65 and 2.79 times higher than those of neat CaTiO₃ and B-CaTiO₃. The better activity of the B-CaTiO₃/5GO nanocomposite is ascribed to the presence of heterojunction and synergistic effect of GO and B in the structure, which can inhibit the electron-hole recombination and transport efficiency of photogenerated charge carriers due to the big surface area and more active photocatalytic sites of GO [35,62]. Figure 8b also shows that the incorporation of GO amounts in higher than 5% can cause a decrease in the light penetration through the GO sheets and thus results in a decrease in the activity of the CaTiO₃ perovskite catalyst for the formation of reactive species (ROS) [63]. Furthermore, Figure 8c shows the TOC removal activity of MB over B-CaTiO₃ and B-CaTiO₃/5GO heterostructure. It is clear that the mineralization ratio of the B-CaTiO₃/5GO heterostructure (60.1%) is better than that of B-CaTiO₃ (12.4%), which shows that the B-CaTiO₃/5GO heterostructure has a far higher mineralization ability and MB is decomposed into smaller molecules and by-products [64,65]. The impact of the initial MB concentration on its degradation over B-CaTiO₃/5GO under visible irradiation degradation tests were performed out by changing the concentration of MB (5–20 mg/L) with a constant amount of catalyst (50 mg). Figure S2 indicates that with increase in the concentration of MB solution from 5 mg/L to 20 mg/L, the photocatalytic degradation of the MB decreased. The effect of catalyst mass on MB photodegradation (Figure S3) was also determined. As the catalyst increases, the amount of dye adsorbed on the surface increases. As the concentration of catalyst increases, the turbidity of the solution may increase and, accordingly, photocatalytic activity may decrease as light is prevented from reaching the catalyst. However, in this study, since B-CaTiO₃ nanopowder was immobilized on the GO surface, there was no turbidity as the concentration of catalyst increased from 0.5 g/L to 2.5 g/L. When the catalyst concentration increased from 0.5 g/L to 2.5 g/L, the removal percentage of MB increased from 79.9% to 98.3%. The photocatalytic degradation kinetics was determined by performing the pseudo first order kinetic model:

$$\ln(C_0/C_t) = kt \quad (3)$$

In the formula, k is the pseudo-first-order reaction rate coefficient (min⁻¹), t is the reaction time (min), and C_0/C_t is normalized MB concentration. Figure 8d shows that the first order reaction kinetic is suitable for the degradation of MB and Figure 8e presents the kinetic constant values of all the prepared catalysts for degradation of MB in a histogram form. Based on the experimental system for the degradation of MB, the reaction rate coefficient increases from 0.0019 min⁻¹ for B-CaTiO₃ to 0.0106 min⁻¹ for the B-CaTiO₃/5GO, more than 5.6 times increase. The comparison between the B-CaTiO₃/5GO composites prepared in this study and other CaTiO₃-modified graphene catalysts is shown in Table 2 [35–37,39].

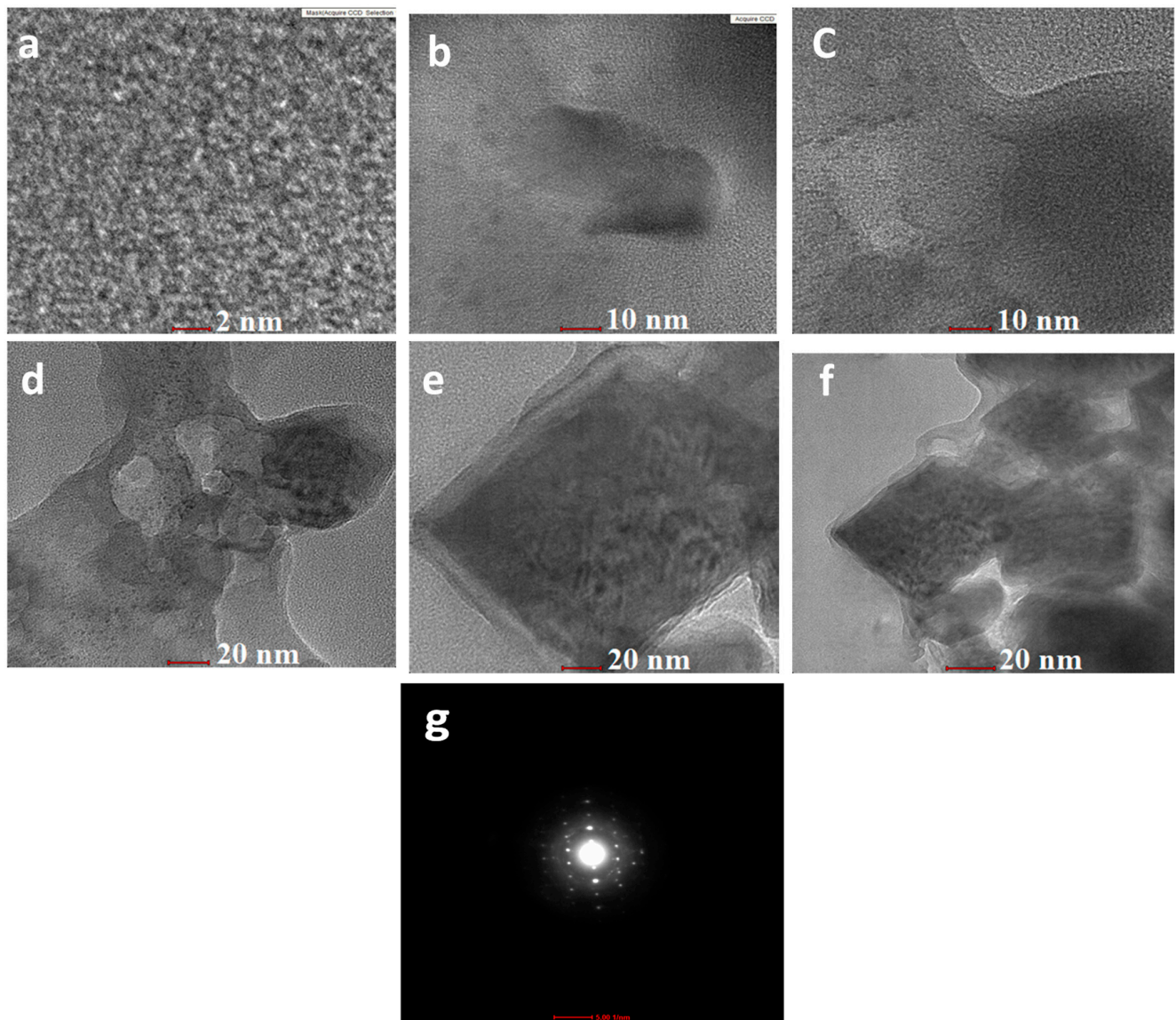
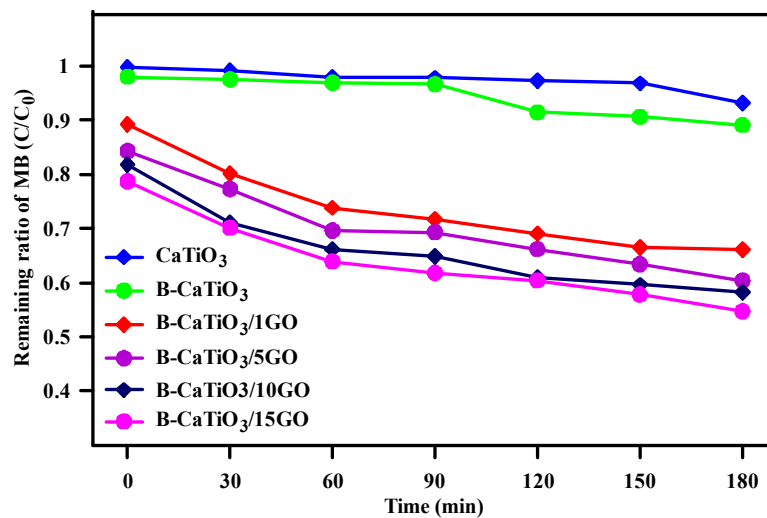


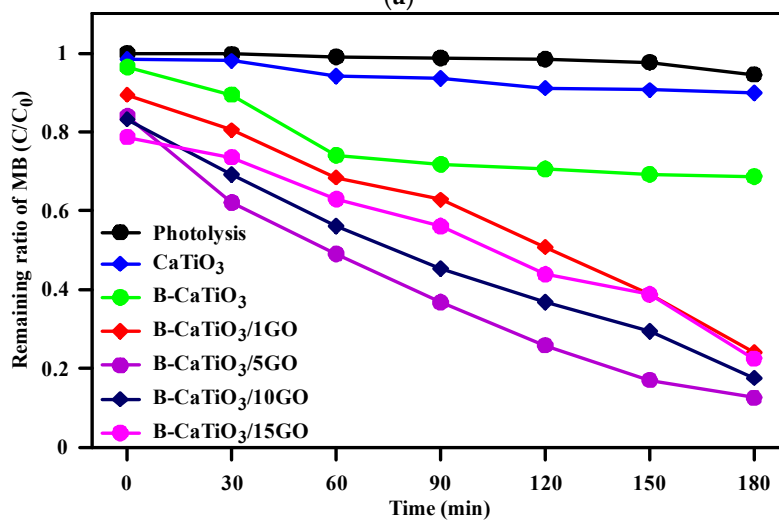
Figure 7. HR-TEM images for B-CaTiO₃/5GO (a–f), and SAED pattern of B-CaTiO₃/5GO (g).

Table 2. Comparison of CaTiO₃ and graphene-activated nanostructures reported by several researchers.

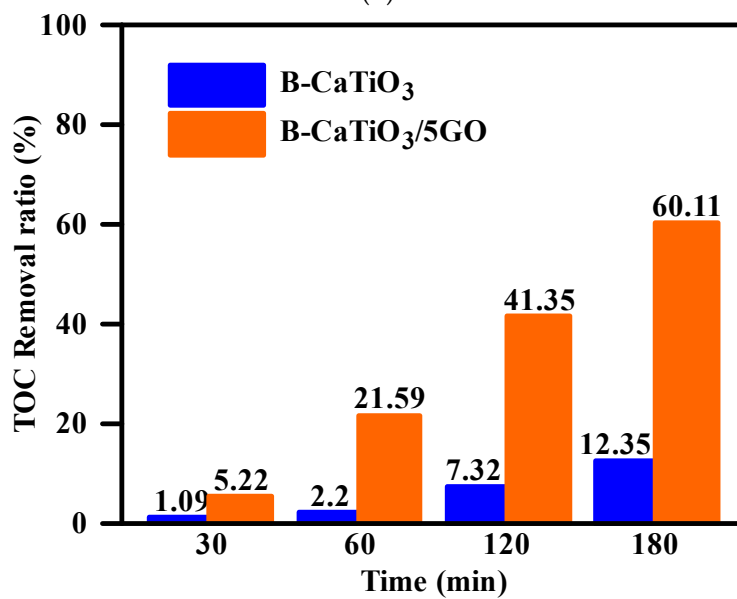
Pollutant	Photocatalyst	Light Source	[Pollutant]	[Catalyst]	% Removal	Time	Refs.
MB	RGO-N-CaTiO ₃	Visible light	4×10^{-5} M	50 mg	~95	180	[30]
Methyl orange	CaTiO ₃ -graphene	UV light	1 mg/L	1 g/L	~98	60	[31]
MB	CaTiO ₃ /rGO/NiFe ₂ O ₄	Sunlight	5 mg/L	0.1 g/L	~83	180	[32]
Methyl orange	CaTiO ₃ /rGO	UV light	5 mg/L	100 mg	~93	60	[34]
MB	B-CaTiO ₃ /5GO	Visible light	10 mg/L	1 g/L	87.4	180	This work



(a)



(b)



(c)

Figure 8. Cont.

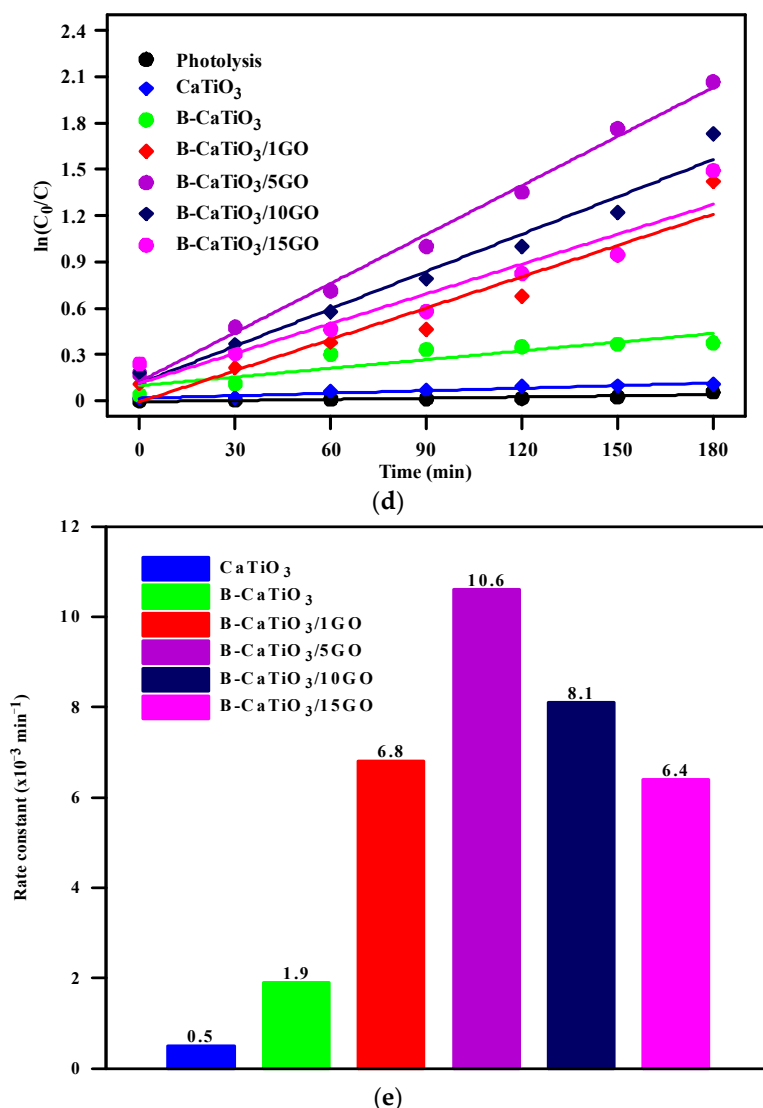


Figure 8. Adsorption of MB (a) and photocatalytic degradation of MB under visible light irradiation (b), TOC removal ratio in 180 min by the B-CaTiO₃ and B-CaTiO₃/5GO (c), kinetic curves of MB degradation (d), and histogram representing the values of the rate constants of all photocatalysts [$C_0 = 10 \text{ mg L}^{-1}$; Catalyst amount = 1 g L^{-1} ; pH 6.05] (e).

3.2.1. Effect of pH

To evaluate the most suitable pH of MB dye solution for its degradation over B-CaTiO₃/5GO, degradation tests were performed in pH range from 3 to 12 during a 180 min treatment period with a constant amount of photocatalyst (50 mg) and initial concentration of MB (10 mg L^{-1}). To evaluate the point of zero charge (pH_{pzc}), zeta potential evaluation was performed as a function of the suspended B-CaTiO₃/5GO sample. It is an important phenomenon that the pollutant to be decomposed is first adsorbed on the catalyst surface, while pH also affects the speciation of ionic species and the properties of the catalyst surface. Figure 9a shows the point of zero charges of the B-CaTiO₃/5GO in water and the pH_{pzc} of B-CaTiO₃/5GO composite was at the pH value of 3.39. This value is close to the value at which commercial CaTiO₃ reaches zero load point at pH 3 [66]. Hence, B-CaTiO₃/5GO surface is positively charged at a lower pH ($\text{pH} < 3.39$), whereas it is negatively charged under alkaline conditions ($\text{pH} > 3.39$) [67,68]. At a pH higher than pH 3.39, the performance of the MB degradation is anticipated to enhance with increasing pH due to the electrostatic interactions between the negatively charged B-CaTiO₃/5GO surface and the MB cations. Figure 9b shows the effect of pH on the degradation of MB by B-CaTiO₃/5GO composite.

The maximum degradation percentage is obtained at pH 6.05 (its natural pH of MB). At the same time, the lower removal efficiency of MB at pH 3.06 may be due to the presence of Cl^- ions formed from the ionization of HCl acid used in pH adjustment. However, the degradation performance did not significantly change between pH 6.05 and 12.08. This can be an advantage because no additional pH arrangement is required for degradation process of MB.

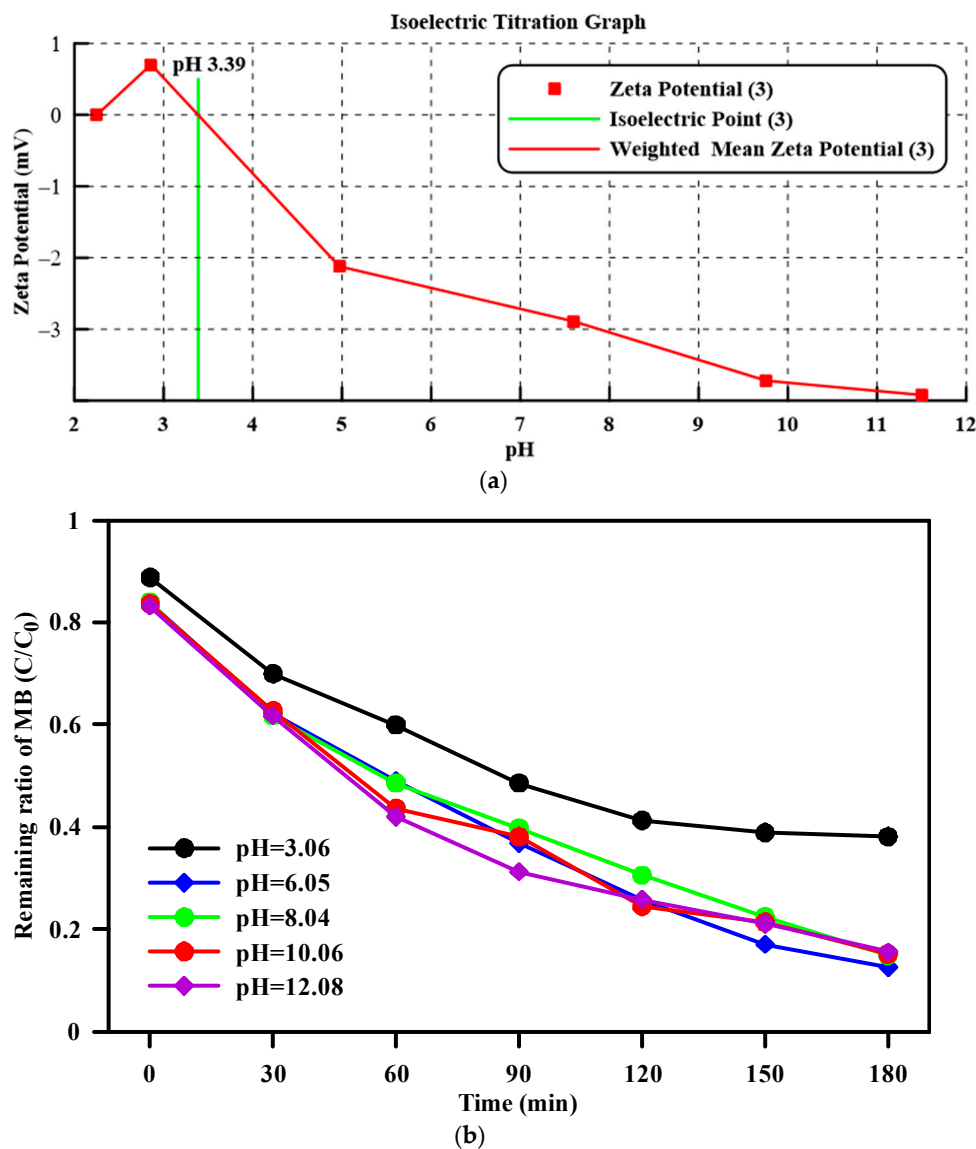


Figure 9. Zeta potential of B-CaTiO₃/5GO at pH between 2 and 12 (a) and the effect of pH on photocatalytic degradation of MB under visible light [$C_0 = 10 \text{ mg L}^{-1}$; B-CaTiO₃/5GO = 1 g L^{-1}] (b).

3.2.2. Effect of Water Matrix

Since real secondary wastewater bodies contain common inorganic ions such as bicarbonate, nitrate, sulfate, and chloride, the influence of co-existing anions (C_0 : 2 mM for all ions) on MB degradation was analyzed. Figure 10a shows that all the coexisting elements cause a decrease in the degradation efficiency of MB. As given in Figure 10a, the presence of bicarbonate, nitrate, sulfate, and chloride showed different blocking effects on the degradation of MB and the corresponding degradation rates are 81.2%, 70.2%, 65.8%, and 77.9%, respectively, starting from 87.4%. The inhibitory effects of coexisting ions may be due to their role as scavengers for reactive oxygen species responsible for degradation. Although these ions have been converted into new radical species, their photocatalytic

performance was less effective than the reactive oxygen species (ROS) [69]. Consequently, the degradation rate of MB may be decreased in the presence of these anions. However, their impacts on decomposition of MB can be assigned to specific experimental parameters such as catalytic reaction procedure, the kind of pollutant and the kind of the catalyst, and so on [70]. As indicated in Figure 10b, the degradation activities were found as 82.2% and 71.4% in terms of tap and sea water, respectively. The data showed that MB removal was adversely affected in the sea water while the degradation rate slightly decreased in the tap water compared to photocatalytic studies with DI water. One of the possible reasons for this decrease may be competitive adsorption between the anions (SO_4^{2-} and Cl^-) in the water matrix and on the surface of the photocatalyst. Another reason for the decrease in photoactivity can be clarification with the interaction of $\cdot\text{OH}$ formed in photocatalytic processes with sulfate and carbonate ions in the aqueous medium. In addition, humic acid (HA), a natural organic substance typically presented in surface water, was used to simulate real water samples. HA may negatively affect the photocatalytic degradation reactions because of the interferences with the ROS during the photocatalytic processes. HA usually presents in surface natural water ranging from 2 to 10 mg/L, so 5 or 8 mg/L HA were tested under the same experimental settings in this study [71]. As seen in Figure 11, the photocatalytic removal of MB slightly decreased in the presence of HA. Particularly, in the case of adding 5 mg/L HA and 8 mg/L HA to the reaction, the MB degradation percentage declined from 87.4% to 79.2% and 71.1%, respectively. Thus, it can be suggested that the adsorption of HA on the photocatalyst surface is competitive with MB and the decrease in the light penetration would be reasons for the decrease in the photocatalytic activity for MB degradation [72]. These facts suggest that the MB degradation is anticipated to be slower in real water samples containing both co-existing ions and HA.

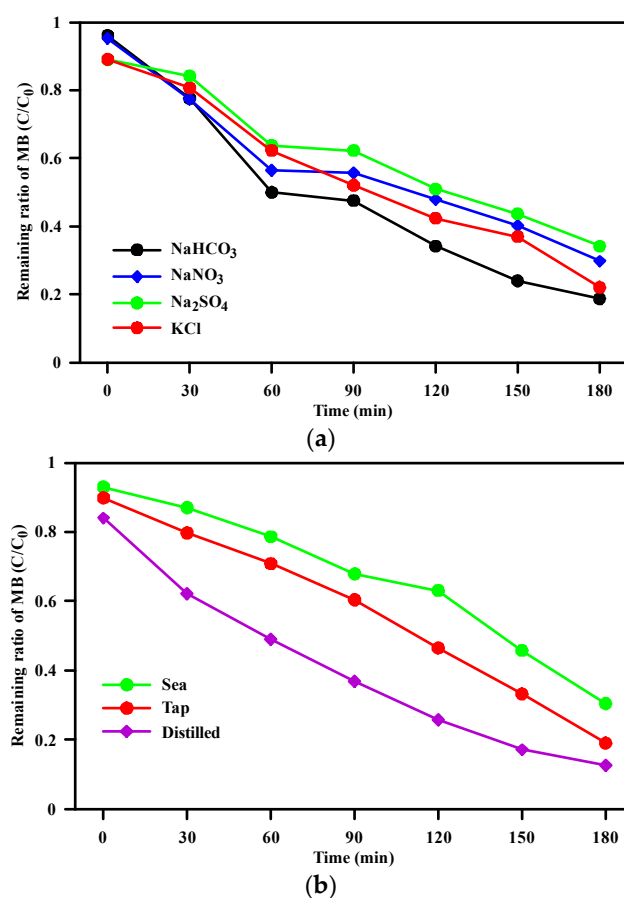


Figure 10. Effect of inorganic anions (a) and water matrix on MB degradation [$C_0 = 10 \text{ mg L}^{-1}$; $\text{B-CaTiO}_3/5\text{GO} = 1 \text{ g L}^{-1}$] (b).

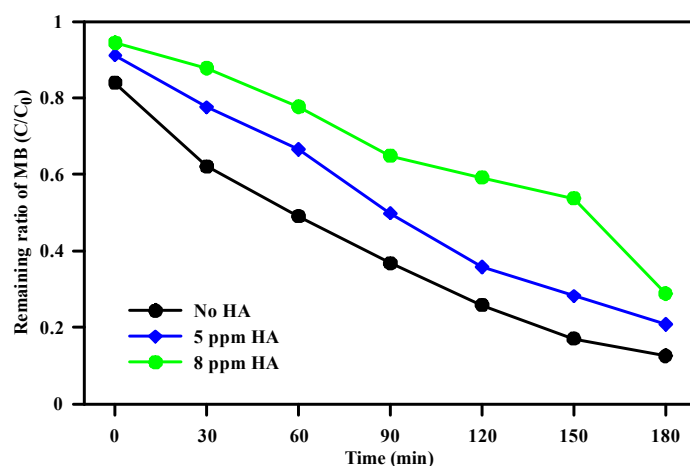
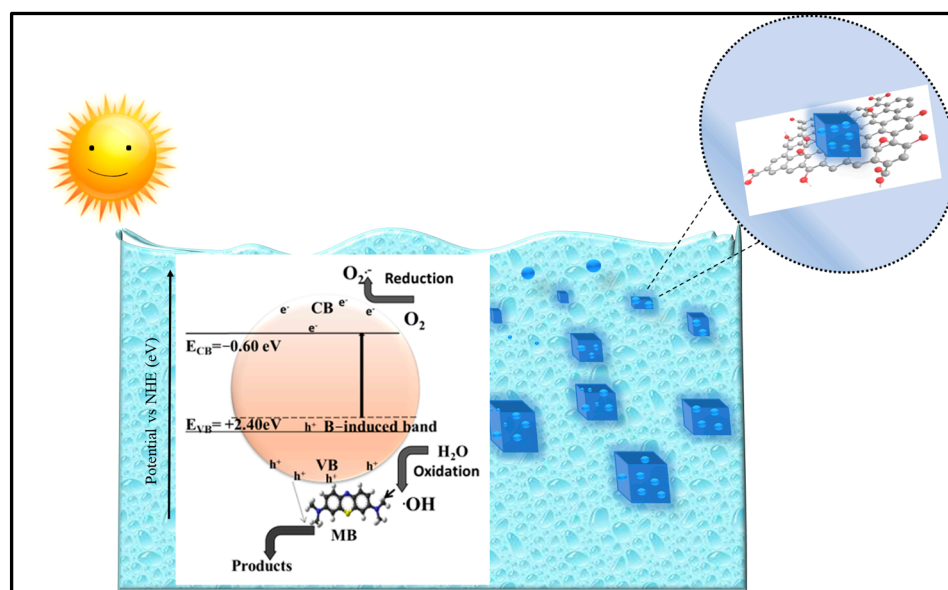


Figure 11. Effect of HA on MB degradation [$C_0 = 10 \text{ mg L}^{-1}$; B-CaTiO₃/5GO = 1 g L^{-1} ; pH 6.05].

3.2.3. Mechanism of Photocatalytic Degradation

The potential mechanism responsible for the degradation of MB by B-CaTiO₃/GO catalyst is given in Scheme 2 and discussed below.



Scheme 2. Schematic illustration of the possible photocatalytic mechanism of B-CaTiO₃/5GO.

The performance of high capability of charge separation and formation of ROS on the surface of B-CaTiO₃/GO nanocomposite during a photocatalytic process have a key role in the improvement of the photocatalytic performance. The band gap of the CaTiO₃ photocatalyst has been reported as 3.5 eV in the literature [73]. In this work, the band gap energies of CaTiO₃, B-CaTiO₃, and B-CaTiO₃/5GO were estimated as 3.33 eV, 2.99 eV, and 2.85 eV, respectively. In B-CaTiO₃/5GO, during light irradiation, the electrons in the valence band are induced from the VB to the CB, with simultaneous formation of holes (h⁺) in the VB. These photoexcited e⁻/h⁺ pairs can be moved to the B-CaTiO₃/5GO catalyst surface and participate in redox reaction. Furthermore, graphene can act as an acceptor of photo-induced electrons from the CB of the B-CaTiO₃ catalyst because of its large specific surface area and high conductivity. These photoexcited electrons react with adsorbed oxygen to form superoxide radical anions (O₂·⁻). At this time, the holes react with H₂O or OH⁻ adsorbed on the surface of the B-CaTiO₃/5GO to generate ·OH radical. These strong oxidative species play a role in the degradation of MB to further degrade or mineralize

MB. To confirm the proposed mechanism and to get an idea of the role performed by ROS, trapping tests were carried out for MB removal using the B-CaTiO₃/5GO photocatalyst under visible irradiation. The trapping experiments results are given in Figure 12.

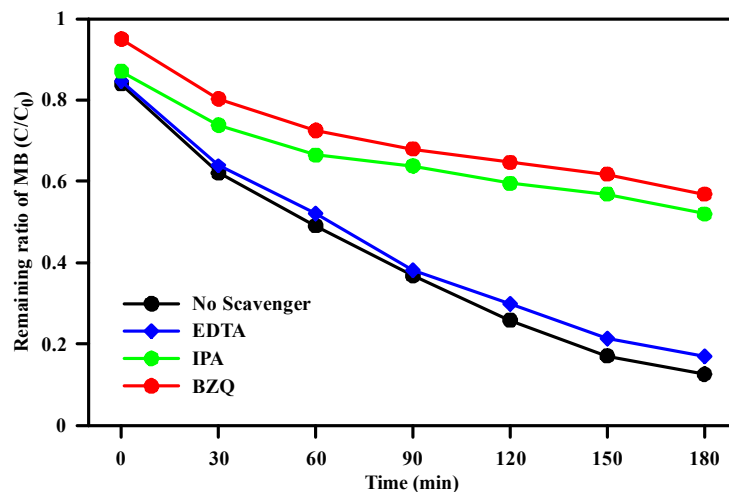


Figure 12. Photocatalytic degradation of MB in the presence of scavengers under visible light [$C_0 = 10 \text{ mg L}^{-1}$; B-CaTiO₃/5GO = 1 g L^{-1} ; pH 6.05].

The photocatalytic removal of MB was dramatically quenched in the presence of BZQ, indicating that the O₂^{·−} radical species was dominant in the degradation experiments (Figure 12). Additionally, a considerable reduction in the degradation rate also occurred in the presence of IPA, indicating the effective role of ·OH radical anions in the degradation of MB. However, h⁺ species do not make a contribution much as the presence of BZQ or IPA and had only a minor active role on the removal of MB. Hence, the above results show that all three species play an active role in the photocatalytic capacity of B-CaTiO₃/5GO in the order O₂^{·−} > ·OH > h⁺. Moreover, to further clarify the redox reactions of photoinduced carries, it is essential to calculate the CB and VB edge potentials of B-CaTiO₃. The CB and VB potentials of B-CaTiO₃ can be estimated using Mulliken electronegativity theory and are estimated to be −0.60 eV and +2.40 eV, respectively (Supplementary Materials) [74]. The VB edge of B-CaTiO₃ (2.40 eV) is close to the redox potential of H₂O/·OH (2.72 V vs. NHE) but is higher positive potential than OH[−]/·OH (+1.89 V vs. NHE) [75]. This suggests that the photoinduced h⁺ can easily react with OH[−] (but not nearly with H₂O) to generate ·OH radicals. Also, the reduction potential of O₂/O₂^{·−} is about −0.13 V versus NHE [76], which is more positive than the potential of the B-CaTiO₃ catalyst. The dissolved O₂ present in the reaction can react with photoinduced e[−] to generate superoxide radical (O₂^{·−}) (Equation (6)). O₂^{·−} is one of the active species leading to dye degradation; it tends to participate more in the reactions defined in Equations (6)–(8). This is one of the alternative ways to generate ·OH radicals, and in this study O₂ is continuously pumped into the reaction and dominant reactive oxygen species because the CB band of B-CaTiO₃ is more negative than the reduction potential of O₂/O₂^{·−}. Scheme 2 schematically shows the photocatalytic mechanism of B-CaTiO₃/5GO for dye degradation.

The general possible photocatalytic reaction mechanism can be summarized as follows Equations (4)–(11) [77]:





3.2.4. Photocatalyst Reusability

It is essential to evaluate the photocatalytic stability and reusability of the catalysts since it could significantly decrease the costs of the photocatalytic operation in water treatment processes and disclose most hopeful photocatalysis candidates. Therefore, five successive cycles of degradation of MB to determine the reusability of the B-CaTiO₃/5GO heterojunction as an effective nanocomposite were carried out. After each MB photocatalytic test was carried out, the precipitates were taken after centrifugation and kept for the next cycle. The results obtained are presented in Figure 13. It can be seen that the degradation rate of MB for the first and fifth cycling has decreased slightly from 87.4% to 82.8%, which may be because of the loss of the catalysts during each test process, which contains some recovery stages such as centrifugation, washing, and drying. However, the high degradation performance of the B-CaTiO₃/5GO photocatalyst shows its high photostability, likely because the adsorbed by-products were decomposed for the following degradation tests.

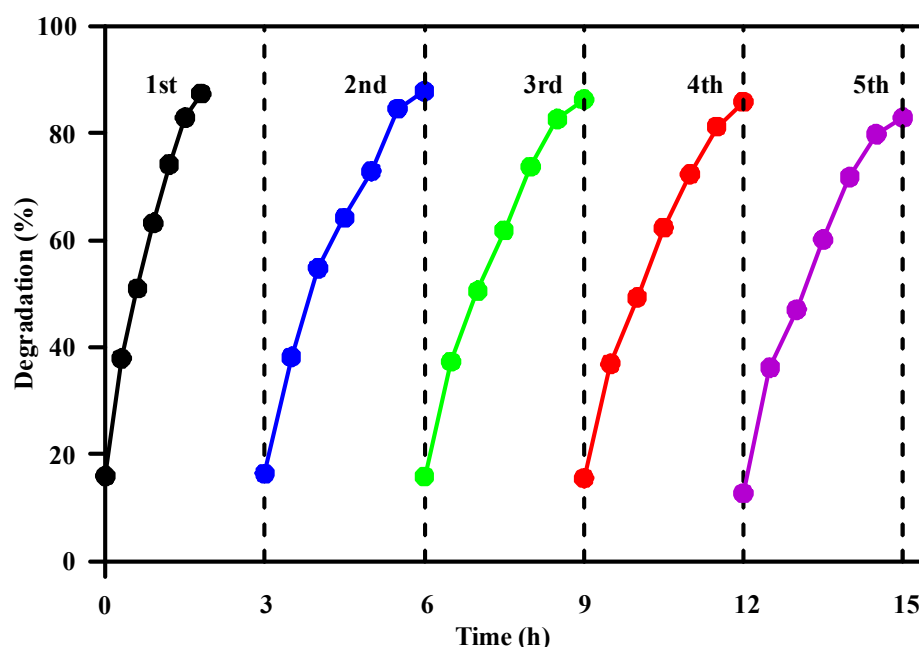


Figure 13. Photocatalyst reusability up to five cycles [$C_0 = 10 \text{ mg L}^{-1}$; B-CaTiO₃/5GO = 1 g L^{-1} ; pH 6.05].

4. Conclusions

In conclusion, a series of boron doped CaTiO₃ were supported on GO nanosheets (B-CaTiO₃/5GO nanocomposites) for the first time and showed their effective visible light driven photocatalysis activity for the decomposition of a colored dye (MB). The B-

CaTiO₃/5GO composite is found to be the most effective nanocomposite among other composites since it has the best degradation efficiency of MB-dyed molecules. It was observed that 31.3% MB photodegraded due to B-CaTiO₃ while 87.4% MB photodegraded due to the B-CaTiO₃/5GO nanocomposite. The increased catalytic efficiency can be corresponded to the incorporation of GO in the composite because the GO has a large surface area and excellent electronic properties to carry charge carrier species. Furthermore, the noteworthy recyclability of the most effective catalyst is also shown. This work could be a good example for a field-based study and feasibility of visible irradiation driven and perovskite-based bifunctional photocatalysts for the environmental remediation.

Supplementary Materials: The following supporting information can be downloaded at: <https://www.mdpi.com/article/10.3390/pr11113191/s1>. Figure S1: N₂ isotherms of (a) B-CaTiO₃ and (b) B-CaTiO₃/5GO catalysts; Figure S2: The effect of initial concentration of MB on photocatalytic removal [Catalyst amount = 1 g L⁻¹; pH 6.05]; Figure S3: The effect of catalyst mass on photocatalytic removal [C₀ = 10 mg L⁻¹; pH 6.05]. Reference [78] is cited in the Supplementary Materials.

Funding: This research received no external funding.

Data Availability Statement: The data that support the findings of this study are available within the article.

Conflicts of Interest: The author declares no conflict of interest.

References

1. Altin, I.; Sökmen, M. Buoyant photocatalyst based on ZnO immobilized on polystyrene beads for pollutants treatment. *Clean Soil Air Water* **2015**, *43*, 974–1113. [CrossRef]
2. Ravichandran, K.; Nithiyadevi, K.; Sakthivel, B.; Arun, T.; Sindhuja, E.; Muruganandam, G. Synthesis of ZnO:Co/rGO nanocomposites for enhanced photocatalytic and antibacterial activities. *Ceram. Int.* **2016**, *42*, 17539–17550. [CrossRef]
3. Vadivelan, V.; Kumar, K.V. Equilibrium, kinetics, mechanism, and process design for the sorption of methylene blue onto rice husk. *J. Colloid Interface Sci.* **2005**, *286*, 90–100. [CrossRef] [PubMed]
4. Li, Y.; Tang, Z.; Zhang, J.; Zhang, Z. Reduced graphene oxide three-dimensionally wrapped WO₃ hierarchical nanostructures as high-performance solar photocatalytic materials. *Appl. Catal. A* **2016**, *522*, 90–100. [CrossRef]
5. Jin, J.; Yu, J.; Guo, D.; Cui, C.; Ho, W. A hierarchical Z-scheme CdS-WO₃ photocatalyst with enhanced CO₂ reduction activity. *Small* **2015**, *11*, 5262–5271. [CrossRef]
6. Huang, H.; Zhao, J.; Bo, W.; Lai, F.; Zhang, M.; Hofkens, J.; Roeyfaers, M.B.J.; Steele, J.A.; Long, J. Site-Sensitive Selective CO₂ Photoreduction to CO over Gold Nanoparticles. *Angew. Chem. Int. Ed.* **2022**, *61*, e202204563. [CrossRef]
7. Sobhani-Nasab, A.; Behvandi, S.; Karimi, M.A.; Sohoul, E.; Karimi, M.S.; Gholipour, N.; Ahmadi, F.; Rahimi-Nasrabadi, M. Synergetic effect of graphene oxide and C₃N₄ as co-catalyst for enhanced photocatalytic performance of dyes on Yb₂(MoO₄)₃/YbMoO₄ nanocomposite. *Ceram. Int.* **2019**, *45*, 17847–17858. [CrossRef]
8. Sobhani-Nasab, A.; Behpour, M.; Rahimi-Nasrabadi, M.; Ahmadi, F.; Pourmasoud, S. New method for synthesis of BaFe₁₂O₁₉/Sm₂Ti₂O₇ and BaFe₁₂O₁₉/Sm₂Ti₂O₇/Ag nano-hybrid and investigation of optical and photocatalytic properties. *J. Mater. Sci. Mater. Electron.* **2019**, *30*, 5854–5865. [CrossRef]
9. Hoffmann, M.R.; Martin, S.T.; Choi, W.; Bahnemann, D.W. Environmental applications of semiconductor photocatalysis. *Chem. Rev.* **1995**, *95*, 69–96. [CrossRef]
10. Anucha, C.B.; Altin, I.; Bacaksiz, E.; Stathopoulos, V.N.; Polat, I.; Yasar, A.; Yüksel, Ö.F. Silver doped zinc stannate (Ag-ZnSnO₃) for the photocatalytic degradation of caffeine under UV irradiation. *Water* **2021**, *13*, 1290. [CrossRef]
11. Xiang, Q.; Yu, J.; Jaroniec, M. Graphene-based semiconductor photocatalysts. *Chem. Soc. Rev.* **2012**, *41*, 782–796. [CrossRef]
12. Anucha, C.B.; Altin, I.; Bacaksiz, E.; Degirmencioglu, I.; Kucukomeroglu, T.; Yilmaz, S.; Stathopoulos, V.N. Immobilized TiO₂/ZnO sensitized copper (II) phthalocyanine heterostructure for the degradation of ibuprofen under UV irradiation. *Separations* **2021**, *8*, 24.
13. Altin, I.; Sökmen, M. Photocatalytic properties of silver incorporated titania nanoparticles immobilized on waste-derived polystyrene. *Water Air Soil Poll.* **2014**, *225*, 1786. [CrossRef]
14. Zhang, L.; Nie, Y.; Hu, C.; Qu, J. Enhanced Fenton degradation of Rhodamine B over nanoscaled Cu-doped LaTiO₃ perovskite. *Appl. Catal. B* **2012**, *125*, 418–424. [CrossRef]
15. Kusanov, Z.; Umirzakov, A.; Serik, A.; Baimenov, A.; Yeleuov, M.; Daubayev, C. Multifunctional strontium titanate perovskite-based composite photocatalysts for energy conversion and other applications. *Int. J. Hydrogen Energy* **2023**, *in press*. [CrossRef]
16. Belousov, A.S.; Parkhacheva, A.A.; Suleimanov, E.V.; Shafiq, I. Potential of Bi₂WO₆-based heterojunction photocatalysts for environmental remediation. *Mater. Today Chem.* **2023**, *32*, 101633. [CrossRef]
17. Wei, K.; Faraj, Y.; Yao, G.; Xie, R.; Lai, B. Strategies for improving perovskite photocatalysts reactivity for organic pollutants degradation: A review on recent progress. *J. Chem. Eng.* **2021**, *414*, 128783. [CrossRef]

18. Djellabi, R.; Ordonez, M.F.; Conte, F.; Falletta, E.; Bianchi, C.L.; Rossetti, I. A review of advances in multifunctional XTiO_3 perovskite-type oxides as piezo-photocatalysts for environmental remediation and energy production. *J. Hazard. Mater.* **2022**, *421*, 126792. [[CrossRef](#)]
19. Bradha, M.; Hussain, S.; Chakravarty, S.; Amarendra, G.; Ashok, A. Total conductivity in Sc-doped LaTiO_3 perovskites. *Ionics* **2014**, *20*, 1343–1350. [[CrossRef](#)]
20. Kim, Y.; Schlegel, H.; Kim, K.; Irvine, J.T.S.; Kim, J.H. X-ray photoelectron spectroscopy of Sm-doped layered perovskite for intermediate temperature-operating solid oxide fuel cell. *Appl. Surf. Sci.* **2014**, *288*, 695–701. [[CrossRef](#)]
21. Hong, H.J.; Yashiro, K.; Hashimoto, S.I. Conduction properties and ionic transference behavior of $\text{CaTi}_{1-x}\text{Sc}_x\text{O}_3$ ($x = 0.05, 0.1$). *ECS Trans.* **2014**, *61*, 151. [[CrossRef](#)]
22. He, Y.; Chong, H.; Qing-Wei, L.I.; Xue, X.X. Effect of baking temperature on photocatalytic properties of titanium calcium. *J. Funct. Mater.* **2010**, *31*, 1297–1299.
23. Wei, Z.; Xiao, W.; Ren, Z.H.; Gang, X.U.; Ge, S.; Zan, Z.; Zhang, Y.F.; Han, G.R. Hydrothermal synthesis and photocatalytic property of CaTiO_3 assisted with sodium citrate. *J. Funct. Mater.* **2012**, *43*, 50–53.
24. Nishimoto, S.; Matsuda, M.; Miyake, M. Photocatalytic activities of Rh-doped CaTiO_3 under visible light irradiation. *Chem. Lett.* **2006**, *35*, 308–309. [[CrossRef](#)]
25. Chen, X.; He, X.; Yang, X.; Wu, Z.; Li, Y. Construction of novel 2D/1D g- C_3N_4 / CaTiO_3 heterojunction with face-to-face contact for boosting photodegradation of triphenylmethane dyes under simulated sunlight. *J. Taiwan Inst. Chem. Eng.* **2020**, *107*, 98–109. [[CrossRef](#)]
26. Huang, S.; Guo, S.; Wang, Q.; Zhu, N.; Lou, Z.; Li, L.; Shan, A.; Yuan, H. CaF_2 -Based near infrared photocatalyst using the multifunctional CaTiO_3 precursors as the calcium source. *ACS Appl. Mater. Interfaces* **2015**, *7*, 20170–20178. [[CrossRef](#)]
27. Bai, L.; Xu, Q.; Cai, Z. Synthesis of $\text{Ag@AgBr}/\text{CaTiO}_3$ composite photocatalyst with enhanced visible light photocatalytic activity. *J. Mater. Sci. Mater. Electron.* **2018**, *29*, 17580–17590. [[CrossRef](#)]
28. Liu, M.; Qiu, X.; Miyauchi, M.; Hashimoto, K. Energy-level matching of Fe(III) ions grafted at surface and doped in bulk for efficient visible-light photocatalysts. *J. Am. Chem. Soc.* **2013**, *135*, 10064–10072. [[CrossRef](#)]
29. Li, C.; Xu, H.; Gao, J.; Du, W.; Shangguan, L.; Zhang, X.; Lin, R.-B.; Wu, H.; Zhou, W.; Liu, X.; et al. Tunable titanium metal–organic frameworks with infinite 1D Ti–O rods for efficient visible-light-driven photocatalytic H_2 evolution. *J. Mater. Chem.* **2019**, *7*, 11928–11933. [[CrossRef](#)]
30. Bell, N.J.; Ng, Y.H.; Du, A.; Coster, H.; Smith, S.C.; Amal, R. Understanding the enhancement in photoelectrochemical properties of photocatalytically prepared TiO_2 -reduced graphene oxide composite. *J. Phys. Chem. C* **2011**, *115*, 6004–6009. [[CrossRef](#)]
31. Du, A.; Ng, Y.H.; Bell, N.J.; Zhu, Z.; Amal, R.; Smith, S.C. Hybrid graphene/titania nanocomposite: Interface charge transfer, hole doping, and sensitization for visible light response. *J. Phys. Chem. Lett.* **2011**, *2*, 894–899. [[CrossRef](#)]
32. Altin, I. CuO-TiO_2 /graphene ternary nanocomposite for highly efficient visible-light-driven photocatalytic degradation of bisphenol A. *J. Mol. Struct.* **2022**, *1252*, 132199. [[CrossRef](#)]
33. Han, W.; Chen, L.; Song, W.; Wang, S.; Fan, X.; Li, Y.; Zhang, F.; Zhang, G.; Peng, W. Synthesis of nitrogen and sulfur co-doped reduced graphene oxide as efficient metal-free cocatalyst for the photo-activity enhancement of CdS . *Appl. Catal. B* **2018**, *236*, 212–221. [[CrossRef](#)]
34. Huo, Y.S.; Yang, H.; Xian, T.; Jiang, J.L.; Wei, Z.Q.; Li, R.S.; Feng, W.J. A polyacrylamide gel route to different-sized CaTiO_3 nanoparticles and their photocatalytic activity for dye degradation. *J. Sol Gel Sci. Technol.* **2014**, *71*, 254–259. [[CrossRef](#)]
35. Kumar, A.; Kumar, S.; Bahuguna, A.; Kumar, A.; Sharma, V.; Krishnan, V. Recyclable, bifunctional composites of perovskite type N- CaTiO_3 and reduced graphene oxide as an efficient adsorptive photocatalyst for environmental remediation. *Mater. Chem. Front.* **2017**, *1*, 2391. [[CrossRef](#)]
36. Xian, T.; Yang, H.; Huo, Y.S. Enhanced photocatalytic activity of CaTiO_3 -graphene nanocomposites for dye degradation. *Phys. Scr.* **2014**, *89*, 115801. [[CrossRef](#)]
37. Chen, X.; Di, L.; Yang, H.; Xian, T. A magnetically recoverable CaTiO_3 /reduced graphene oxide/ NiFe_2O_4 nanocomposite for the dye degradation under simulated sunlight irradiation. *J. Ceram. Soc. Jpn.* **2019**, *127*, 221–231. [[CrossRef](#)]
38. Lalan, V.; Pillai, V.P.M.; Gopchandran, K.G. Enhanced electron transfer due to rGO makes Ag-CaTiO_3 @rGO a promising plasmonic photocatalyst. *J. Sci. Adv. Mater. Dev.* **2022**, *7*, 100468. [[CrossRef](#)]
39. Luo, P.; Liu, W.; Zhu, D.; Sun, B.; Cao, Y.; Wang, Y. One-step synthesis of Ti^{3+} self-doped CTO/rGO composites by pulsed laser ablation in liquid with enhanced photocatalytic activity in water purification. *Colloids Surf. A Physicochem. Eng. Asp.* **2022**, *655*, 130216. [[CrossRef](#)]
40. Kudo, A.; Miseki, Y. Heterogeneous photocatalyst materials for water splitting. *Chem. Soc. Rev.* **2009**, *38*, 253–278. [[CrossRef](#)]
41. Choi, C.H.; Chung, M.W.; Kwon, H.C.; Park, S.H.; Woo, S.I. B, N- and P, N-doped graphene as highly active catalysts for oxygen reduction reactions in acidic media. *J. Mater. Chem. A* **2013**, *1*, 3694–3699. [[CrossRef](#)]
42. Feng, W.; Lei, Y.; Wu, X.; Yuan, J.; Chen, J.; Xu, D.; Zhang, X.; Zhang, S.; Liu, P.; Zhang, L.; et al. Tuning the interfacial electronic structure via Au clusters for boosting photocatalytic H_2 evolution. *J. Mater. Chem. A* **2021**, *9*, 1759–1769. [[CrossRef](#)]
43. Mu, J.; Sun, W.; Li, F.; Guan, Y.; Zhou, X.; Li, J.; Chen, L. Upconversion luminescent perovskite $\text{CaTiO}_3:\text{Yb}^{3+}/\text{Er}^{3+}$ nanocubes. *J. Alloys Compd.* **2019**, *797*, 1002–1006. [[CrossRef](#)]
44. Hummers, W.S.; Offeman, R.E. Preparation of graphitic oxide. *J. Am. Chem. Soc.* **1958**, *80*, 1339. [[CrossRef](#)]
45. Slater, J.C. Atomic Radii in Crystals. *J. Chem. Phys.* **1964**, *41*, 3199–3204. [[CrossRef](#)]

46. Chen, Q.; Liu, H.; Xin, Y.; Cheng, X. TiO₂ nanobelts-effect of calcination temperature on optical, photoelectrochemical and photocatalytic properties. *Electrochim. Acta* **2013**, *111*, 284–291. [[CrossRef](#)]
47. Xu, L.; Yang, L.; Johansson, E.M.J.; Wang, Y.; Jin, P. Photocatalytic activity and mechanism of bisphenol a removal over TiO₂-x/rGO nanocomposite driven by visible light. *Chem. Eng. J.* **2018**, *350*, 1043–1055. [[CrossRef](#)]
48. Bajorowicz, B.; Reszczynska, J.; Lisowski, W.; Klimczuk, T.; Winiarski, M.; Słoma, M.; Zaleska-Medynska, A. Perovskite-type KTaO₃-reduced graphene oxide hybrid with improved visible light photocatalytic activity. *RSC Adv.* **2015**, *5*, 91315–91325. [[CrossRef](#)]
49. Attou, L.; Al-Shami, A.; Boujemaâ, J.; Mounkachi, O.; Ez-Zahraouy, H. Predicting the structural, optoelectronic, dynamical stability and transport properties of Boron-doped CaTiO₃: DFT based study. *Phys. Scr.* **2022**, *97*, 115808. [[CrossRef](#)]
50. Wang, Y.; Niu, C.G.; Wang, L.; Wang, Y.; Zhang, X.G.; Zeng, G.M. Synthesis of fern-like Ag/AgCl/CaTiO₃ plasmonic photocatalysts and their enhanced visible-light photocatalytic properties. *RSC Adv.* **2016**, *6*, 47873–47882. [[CrossRef](#)]
51. Dong, G.; Xiao, X.; Zhang, L.; Ma, Z.; Bao, X.; Peng, M.; Zhang, Q.; Qiu, J. Preparation and optical properties of red, green and blue afterglow electrospun nanofibers. *J. Mater. Chem.* **2011**, *21*, 2194–2203. [[CrossRef](#)]
52. Zheng, H.; Györgyfalva, G.C.; Quimby, R.; Bagshaw, H.; Ubc, R.; Reaney, I.; Yarwood, J. Raman Spectroscopy of B-Site Order-Disorder in CaTiO₃-Based Microwave Ceramics. *J. Eur. Ceram. Soc.* **2003**, *23*, 2653–2659. [[CrossRef](#)]
53. Liu, H.; Zhang, G.; Zhou, Y.; Gao, M.; Yang, F. One-step potentiodynamic synthesis of poly(1,5-diaminoanthraquinone)/reduced graphene oxide nano hybrid with improved electrocatalytic activity. *J. Mater. Chem. A* **2013**, *1*, 13902–13913. [[CrossRef](#)]
54. Altin, I.; Ma, X.; Boffa, V.; Bacaksiz, E.; Magnacca, G. Hydrothermal preparation of B-TiO₂-graphene oxide ternary nanocomposite, characterization and photocatalytic degradation of bisphenol A under simulated solar irradiation. *Mater. Sci. Semicond. Process* **2021**, *123*, 105591. [[CrossRef](#)]
55. Park, B.G. Photoluminescence of Eu³⁺-doped CaTiO₃ perovskites and their photocatalytic properties with a metal ion loading. *Chem. Phys. Lett.* **2019**, *722*, 44–49. [[CrossRef](#)]
56. Han, C.; Liu, J.; Yang, W.; Wu, Q.; Yang, H.; Xue, X. Enhancement of photocatalytic activity of CaTiO₃ through HNO₃ acidification. *J. Photochem. Photobiol. A* **2016**, *322*, 1–9. [[CrossRef](#)]
57. Feng, N.; Zheng, A.; Wang, Q.; Ren, P.; Gao, X.; Liu, S.B.; Shen, Z.; Chen, T.; Deng, F. Boron environments in B-doped and (B, N) codoped TiO₂ photocatalysts: A combined solid-state NMR and theoretical calculation study. *J. Phys. Chem. C* **2011**, *115*, 2709–2719. [[CrossRef](#)]
58. Quinones, D.H.; Rey, A.; Alvarez, P.M.; Beltran, F.J.; Puma, G.L. Boron doped TiO₂ catalysts for photocatalytic ozonation of aqueous mixtures of common pesticides: Diuron, o-phenylphenol, MCPA and terbuthylazine. *Appl. Catal. B* **2015**, *178*, 74–81. [[CrossRef](#)]
59. Tan, H.; Zhao, Z.; Zhu, W.-B.; Coker, E.N.; Li, B.; Zheng, M.; Yu, W.; Fan, H.; Sun, Z. Oxygen vacancy enhanced photocatalytic activity of perovskite SrTiO₃. *ACS Appl. Mater. Interfaces* **2014**, *6*, 19184–19190. [[CrossRef](#)]
60. Kumar, S.; Sharma, V.; Bhattacharyya, K.; Krishnan, V. Synergetic effect of MoS₂-RGO doping to enhance the photocatalytic performance of ZnO nanoparticles. *New J. Chem.* **2016**, *40*, 5185–5197. [[CrossRef](#)]
61. Jiang, E.; Song, N.; Che, G.; Liu, C.; Dong, H.; Yang, L. Construction of a Z-scheme MoS₂/CaTiO₃ heterostructure by the morphology-controlled strategy towards enhancing photocatalytic activity. *Chem. Eng. J.* **2020**, *399*, 125721. [[CrossRef](#)]
62. Chen, D.M.; Yang, D.; Wang, Q.; Jiang, Z.Y. Effects of boron doping on photocatalytic activity and microstructure of titanium dioxide nanoparticles. *Ind. Eng. Chem. Res.* **2006**, *45*, 4110–4116. [[CrossRef](#)]
63. Pan, J.; Zhang, X.; Du, A.; Sun, D.; Leckie, J.O. Self-etching reconstruction of hierarchically mesoporous F-TiO₂ hollow microspherical photocatalyst for concurrent membrane water purifications. *J. Am. Chem. Soc.* **2008**, *130*, 11256–11257. [[CrossRef](#)] [[PubMed](#)]
64. Houas, A.; Lachheb, H.; Ksibi, M.; Elaloui, E.; Guillard, C.; Herrmann, J.M. Photocatalytic degradation pathway of methylene blue in water. *Appl. Catal. B Environ.* **2001**, *31*, 145–157. [[CrossRef](#)]
65. Liu, C.; Lü, H.; Yu, C.; Ding, B.; Ye, R.; Ji, Y.; Dai, B.; Liu, W. Novel FeWO₄/WO₃ nanoplate with p-n heterostructure and its enhanced mechanism for organic pollutants removal under visible-light illumination. *J. Environ. Chem. Eng.* **2020**, *8*, 104044. [[CrossRef](#)]
66. Coreño, J.; Coreño, O. Evaluation of calcium titanate as apatite growth promoter. *J. Biomed. Mater. Res. Part A* **2005**, *75*, 478–484. [[CrossRef](#)]
67. Fan, X.; Zhang, G.; Zhang, F. Multiple roles of graphene in heterogeneous catalysis. *Chem. Soc. Rev.* **2015**, *44*, 3023–3303. [[CrossRef](#)]
68. Lightcap, I.V.; Kosel, T.H.; Kamat, P.V. Anchoring semiconductor and metal nanoparticles on a two-dimensional catalyst mat. storing and shuttling electrons with reduced graphene oxide. *Nano Lett.* **2010**, *10*, 577–583. [[CrossRef](#)]
69. Gao, X.; Guo, Q.; Tang, G.; Peng, W.; Luo, Y.; He, D. Effects of inorganic ions on the photocatalytic degradation of carbamazepine. *J. Water Reuse Desalin.* **2019**, *9*, 301–309. [[CrossRef](#)]
70. Petala, A.; Frontistis, Z.; Antonopoulou, M.; Konstantinou, I.; Kondarides, D.I.; Mantzavinos, D. Kinetics of ethyl paraben degradation by simulated solar radiation in the presence of N-doped TiO₂ catalysts. *Water Res.* **2015**, *81*, 157–166. [[CrossRef](#)]
71. Wang, C.; Zhu, L.; Wei, M.; Chen, P.; Shan, G. Photolytic reaction mechanism and impacts of coexisting substances on photodegradation of bisphenol A by Bi₂WO₆ in water. *Water Res.* **2012**, *46*, 845–853. [[CrossRef](#)] [[PubMed](#)]

72. Antonopoulou, M.; Skoutelis, C.G.; Daikopoulos, C.; Deligiannakis, Y.; Konstantinou, I.K. Probing the photolytic-photocatalytic degradation mechanism of DEET in the presence of natural or synthetic humic macromolecules using molecular-scavenging techniques and EPR spectroscopy. *J. Environ. Chem. Eng.* **2015**, *3*, 3005–3014. [[CrossRef](#)]
73. Kumar, A.; Schuerings, C.; Kumar, S.; Kumar, A.; Krishnan, V. Perovskite-structured CaTiO₃ coupled with g-C₃N₄ as a hetero-junction photocatalyst for organic pollutant degradation. *Beilstein J. Nanotechnol.* **2018**, *9*, 671–685. [[CrossRef](#)] [[PubMed](#)]
74. Wang, S.; Li, D.; Sun, C.; Yang, S.; Guan, Y.; He, H. Synthesis and characterization of g-C₃N₄/Ag₃VO₄ composites with significantly enhanced visible-light photocatalytic activity for triphenylmethane dye degradation. *Appl. Catal. B* **2014**, *144*, 885–892. [[CrossRef](#)]
75. Tachikawa, T.; Fujitsuka, M.; Majima, T. Mechanistic insight into the TiO₂ photocatalytic reactions: Design of new photocatalysts. *J. Phys. Chem. C* **2007**, *111*, 5259–5275. [[CrossRef](#)]
76. Arai, T.; Yanagida, M.; Konishi, Y.; Iwasaki, Y.; Sugihara, H.; Sayama, K. Efficient Complete Oxidation of Acetaldehyde into CO₂ over CuBi₂O₄/WO₃ Composite Photocatalyst under Visible and UV Light Irradiation. *J. Phys. Chem. C* **2007**, *111*, 7574–7577. [[CrossRef](#)]
77. Passi, M.; Pal, B. Influence of Ag/Cu photodeposition on CaTiO₃ photocatalytic activity for degradation of Rhodamine B dye. *Korean J. Chem. Eng.* **2022**, *39*, 942–953. [[CrossRef](#)]
78. Andersen, T.; Haugen, H.K.; Hotop, H. Binding energies in atomic negative ions: III. *J. Phys. Chem. Ref. Data* **1999**, *28*, 1511–1533. [[CrossRef](#)]

Disclaimer/Publisher’s Note: The statements, opinions and data contained in all publications are solely those of the individual author(s) and contributor(s) and not of MDPI and/or the editor(s). MDPI and/or the editor(s) disclaim responsibility for any injury to people or property resulting from any ideas, methods, instructions or products referred to in the content.